Available online at www.sciencedirect.com

ScienceDirect

Geochimica et Cosmochimica Acta 272 (2020) 1–20

Geochimica et Cosmochimica Acta

www.elsevier.com/locate/gca

Transformation of amorphous precursor to crystalline carbonate: Insights from Mg isotopes in the dolomite-analogue mineral norsethite [$BaMg(CO_3)_2$]

Chuan Liu, Weiqiang Li *

State Key Laboratory for Mineral Deposits Research, School of Earth Sciences and Engineering, Nanjing University, Nanjing, Jiangsu 210093, PR China

Received 7 August 2019; accepted in revised form 21 December 2019; Available online 31 December 2019

Abstract

Crystallization from an amorphous precursor is an important pathway of carbonate precipitation in nature. However, the mechanistic details of the transformation from an amorphous phase to a crystalline phase of carbonates remain a topic of intense debate. Two competing mechanisms, including solid-state transition and coupled dissolution-reprecipitation, have been proposed to explain this transformation process. Magnesium is a common element in carbonate crystal lattices and its isotopes may provide unique insights into this problem. In this study, we investigated the transformation of the amorphous carbonate (AC) precursor for norsethite [$BaMg(CO_3)_2$], a dolomite analogue mineral, by *in situ* XRD analysis and isotope exchange experiments using a ^{25}Mg enriched tracer coupled with high precision isotope analyses of $\delta^{26}Mg$ and $\delta^{25}Mg$ values for aqueous and solid phases. *In situ* XRD experiments revealed that the AC can transformed to crystalline norsethite at various temperatures (25 °C, 50 °C and 70 °C) and no intermediate mineral formed during the AC transformation process. ^{25}Mg tracers indicated that near-complete Mg isotope exchange occurred in all exchange experiments during AC transformation. More importantly, after the AC transformation, the system showed surprising apparent non-mass dependent fractionation relationship, that the $\delta^{25}Mg$ value of solid phase became greater than that of aqueous solution from a lower value, producing positive $\Delta^{25}Mg_{solid\text{-}aq}$ fractionation, whereas the $\Delta^{26}Mg_{solid\text{-}aq}$ fractionation remained negative. We numerically modeled the behavior of Mg isotopes (in both $\delta^{26}Mg$ and $\delta^{25}Mg$) for the experimental system according to the two competing mechanisms of AC transformation. The modeling results suggest that the apparent non-mass dependent isotope behavior can only be explained by the coupled dissolution-reprecipitation process. Therefore, this study does not support the solid-state transition mechanism for AC transformation. Further, this study rigorously proves that norsethite can form by precipitation from aqueous solution without replacement, and implies that Mg^{2+} in aqueous solutions can be efficiently dehydrated and incorporated into a well ordered dolomite-group mineral (norsethite) under abiotic, low temperature conditions, thus providing new insights for understanding dolomite precipitation in nature.

Keywords: Amorphous carbonate; Norsethite; ^{25}Mg tracer; Transformation; Isotope exchange; Three-isotope method

1. INTRODUCTION

Amorphous carbonate (AC) is a type of hydrated, poorly ordered, and metastable nanoparticulate material that widely occurs as an intermediate phase in processes of inorganic carbonate precipitation and biomineralization

* Corresponding author.
E-mail address: liweiqiang@nju.edu.cn (W. Li).

https://doi.org/10.1016/j.gca.2019.12.027
0016-7037/

(Weiner et al., 2003; Briones et al., 2008; Gago-Duport et al., 2008; Cartwright et al., 2012; Mass et al., 2017). Amorphous calcium carbonate (ACC), in particular, has attracted considerable attention because its transition to crystalline carbonates is an important and common pathway of carbonate formation in nature. Moreover, carbonate precipitation via the ACC precursor may lead to variations in isotopic ratios of O (Demeny et al., 2016) and Mg (Mavromatis et al., 2017b) in carbonates. Therefore, for better applications of the stable isotope proxies in carbonate geological records, it is necessary to understand the isotopic effects associated with transformation of AC.

Two mechanisms have been proposed to explain the transformation of amorphous carbonate to crystalline carbonates. Some researchers have suggested that carbonate mineralization could proceed by solid-state transition of AC dehydration and structural adjustment (Addadi et al., 2003; Politi et al., 2008; Weiner and Addadi, 2011; Gong et al., 2012). Others have suggested that transformation of AC is a coupled dissolution-reprecipitation process (Ogino et al., 1987; Lee et al., 2008; Rodriguez-Blanco et al., 2012; Giuffre et al., 2015; Rodriguez-Navarro et al., 2015; Purgstaller et al., 2016). These two different mechanisms could have distinct responses in the exchange of ions between the solid and the surrounding fluids. If the transformation of AC is a solid-state transition process, the final crystalline product would inherit the cations from the amorphous precursor. By contrast, the transformation of AC via coupled dissolution-reprecipitation would result in extensive cation exchange between the solid and aqueous phases. Distinguishing the two mechanisms is particularly important for applications of elemental and isotopic signatures in carbonates as paleo-environmental proxies or indicators of geological processes.

In order to further understand the mechanisms of carbonate precipitation via an intermediate amorphous precursor, we chose the Mg^{2+}-Ba^{2+}-CO_3^{2-}-H_2O system and studied the formation of norsethite [$BaMg(CO_3)_2$]. Norsethite has a lattice structure similar to dolomite (Lippmann, 1967), as Mg and O atoms in both minerals form a 6-fold coordinated Mg-O octahedra, and both minerals exhibit alternation of the monolayers of Mg-O and X-O polyhedron (where X is Ca for dolomite and Ba for norsethite). Dolomite is notoriously difficult to precipitate abiotically at ambient conditions (Land, 1998) despite of decades of intense studies (e.g., Burns et al., 2000; Warren, 2000). However, successful synthesis of norsethite at ambient conditions had been achieved (Hood et al., 1974; Morrow and Ricketts, 1986; Pimentel and Pina, 2014), and the occurrence of Mg- and Ba-bearing amorphous phase has been reported to precede crystalline norsethite formation (Pimentel and Pina, 2016). In addition, Mg is a major element in geological materials, including common carbonate minerals such as calcite and dolomite. Mg^{2+} is also a common constituent in natural AC that can increase the stability of AC (Raz et al., 2000, 2003; Politi et al., 2010; Rodriguez-Blanco et al., 2012; Purgstaller et al., 2017). We focused on the behavior of Mg isotopes during the transformation from AC to crystalline norsethite and designed exchange experiments to test the two competing models for crystallization of amorphous carbonate by Mg isotope tracers. Due to the structural similarity between the lattices of norsethite and dolomite, the experimental results may also provide new clues to understand dolomite precipitation in nature.

2. EXPERIMENTAL DESIGN AND METHODS

We conducted systematic mineralogical and isotopic studies, including *in situ* XRD investigations of AC transformation, and a set of isotope exchange experiments that involved an enriched ^{25}Mg tracer. The *in situ* experiments were performed to understand the reaction pathway of norsethite formation and to characterize the mineralogical features of solid products. Additionally, solid and aqueous phases from the isotope exchange experiments were systematically sampled in a time-series for Mg isotope analyses, as well as characterization of the solution chemical compositions throughout the reactions.

For the experiments, reagent grade salts of $MgCl_2{\cdot}6H_2O$, $BaCl_2{\cdot}2H_2O$, and Na_2CO_3, deionized water (=18.2 $M\Omega{\cdot}cm^{-1}$), and an enriched ^{25}Mg spike (^{24}Mg: 0.80%, ^{25}Mg: 98.88%, ^{26}Mg: 0.32%) were used to prepare the reactant solutions, including "solution A" (2 M isotopically normal $MgCl_2$), "solution B" (1 M $BaCl_2$), "solution C" (1 M Na_2CO_3), and "solution D" (2 M $MgCl_2$, enriched in ^{25}Mg, with a $\Delta^{25}Mg' \approx 80‰$, where $\Delta^{25}Mg' = \delta^{25}Mg - 0.5*\delta^{26}Mg$).

2.1. Synthesis of Ba-Mg AC

Synthesis of Ba-Mg AC was undertaken at room temperature. 1 mL of "solution A", 1 mL of "solution B", 2 mL of "solution C", and 6 mL of deionized water were mixed in a 15 mL plastic centrifuge tube. Immediately following the mixing, a white cloudy precipitation was observed to occur in the aqueous solution. The tube was immediately centrifuged at 3000 rpm for 5 minutes to separate the solid and liquid phases, and the solid was further washed with de-ionized water and centrifuged three times to remove interstitial fluids. Aliquots of the washed solid were dissolved in 2% HNO_3 to measure the Mg and Ba contents.

2.2. *In situ* XRD investigation of AC transformation

0.5 mL of "solution A" and 5.5 mL of deionized water were added to the plastic centrifuge tubes and mixed with the AC thoroughly to make a slurry. A tiny fraction (approximately 7 μL) of the slurry was promptly loaded into the micro glass reaction tube using a micro-pipette. The micro glass reaction tube was made by burning a glass tube (0.9 mm inner diameter and 1.0 mm outer diameter) in an oxyhydrogen flame to seal one end. Next, the open end of the micro glass reaction tube was sealed using oxyhydrogen flame. Finally, the sealed micro glass reaction tube was placed onto the heating stage on a Rigaku Rapid II micro X-ray diffractometer. The temperature of the heating stage was set at 25 °C, 50 °C, and 70 °C, and *in situ* XRD

measurement of the reaction product was performed immediately after loading of the micro reaction tube. These experiments were noted as Situ25, Situ50, and Situ70, respectively. The setup of *in situ* XRD analysis is shown in Fig. 1 and Appendix Fig. S1. A Mo-sourced X-ray ($K_\alpha = 0.7093$ Å) was used for better penetration through the glass wall of the micro reaction tube. The diffracted X-ray signals were continuously collected by a 2-D detector of the Rigaku Rapid II micro X-ray diffractometer, and the integrated XRD pattern was read and refreshed every 10 minutes. Other parameters of the XRD instruments are provided in Section 2.4.

2.3. Exchange experiments

The concept of exchange experiments followed a published study of Li et al. (2015). The whole experimental procedure was identical to that described in Section 2.2, except

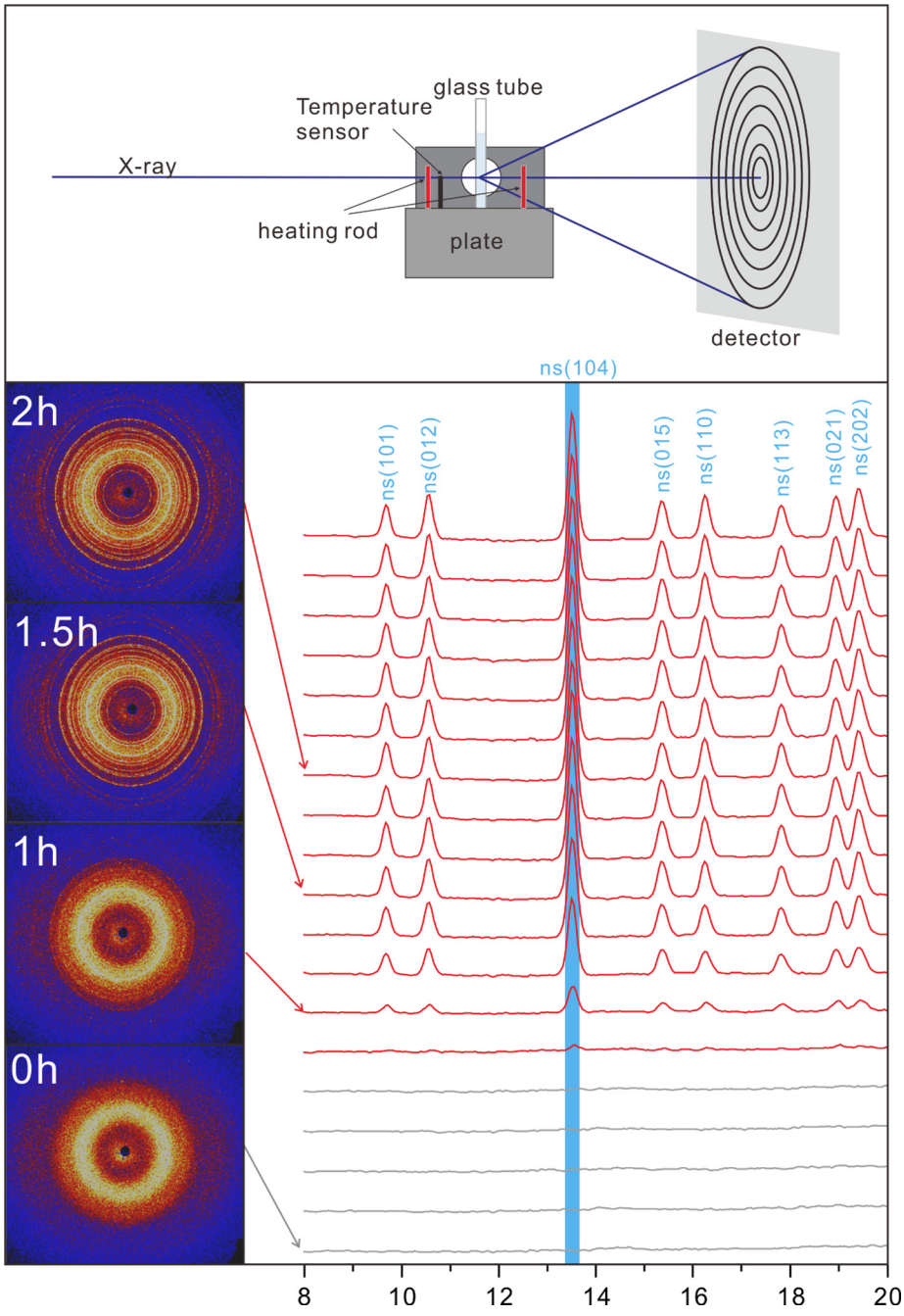

Fig. 1. The setup (top) and the data (bottom) of the *in situ* XRD experiment (Situ70). The Debye rings and diffractograms were taken from 0 h to 3 h of reaction at 70 °C. Blue vertical band denotes norsethite (ns). (For interpretation of the references to colour in this figure legend, the reader is referred to the web version of this article.)

that the "solution A" was substituted by the isotopically enriched "solution D" for mixing with the AC. The initial mass of Mg in the AC and solution was both approximately 0.001 mole. The mixture was placed in a cold-seal stainless steel hydrothermal bomb with a 17 mL PFA inner liner. At least six parallel duplicate experimental vessels were prepared each time individually. The hydrothermal bombs were placed in an oven with the temperature preset to 130 °C (experiment series: Ex130-1 and Ex130-2), and the bombs were sampled in a time series one by one. For experiments conducted at 50 °C and 70 °C (experiment series: Ex50 and Ex70, respectively), centrifuge tubes were used as the reaction vessel and all the tubes were kept rotated in an oven that was equipped with a rotation device. When the bomb or tube was sampled from the oven, it took less than 20 s to open and close the oven, which produced a < 5 °C transient drop in air temperature in the oven. The experimental product was subsequently transferred to a second acid-leached centrifuge tube, which was centrifuged at 3000 rpm for 5 minutes to separate the solid and liquid phases, and the former was further washed with de-ionized water and centrifuged three times to remove interstitial fluids. The supernatant was centrifuged at 12000 rpm for 1 minute before transfer to another acid-leached centrifuge tube. This operation was repeated for three times to remove all the possible suspending solids from the aqueous solution.

2.4. Mineral characterization

The morphology of the solid products was imaged using either a Carl Zeiss Supra 55 Field Emission Scanning Electron Microscope or a Hitachi SU1510 tungsten filament Scanning Electron Microscope, the chemical compositions of the solids were characterized using Energy-Dispersive X-ray Spectroscopy (EDS) with the SEMs.

The XRD analysis was performed on a rotating anode dual source Rigaku Rapid II X-ray diffraction system, using a Mo ($K_\alpha = 0.7093$ Å) target X-ray source running at 50 kV and 90 mA, and a 0.1 mm diameter beam. Powder material was loaded in a Kapton tube for transmission-mode XRD analysis with an exposure time of 10 minutes. Diffraction data were collected on a 2-D image-plate detector, and were converted to the conventional 2θ versus intensity patterns using a Rigaku 2DP software. A Jade 6.5 software was used to interpret the XRD patterns.

2.5. Solution chemistry characterization

Aqueous Ba and Mg concentrations were measured by inductively optical emission spectroscopy (a Skyray ICP3000 type ICP-OES) with a series of gravimetrically prepared multi-element standard solutions. The analytical uncertainty of ICP-OES for elemental analyses was better than ±5%. The total alkalinity was determined by a Brand Titrette titrator with a 0.019 M HCl solution. And the pH of solutions was measured by Mettler Toledo combined a semi-micro glass electrode, which was calibrated against with buffer standard solutions at pH 4.01, 7.00 and 9.21 (analytical uncertainty: ±0.02 pH units).

A PHREEQC software was used to calculate the speciation of aqueous solutions, ion activities and saturation degrees of minerals with its minteq.v4 database. For all experiments, the pH values were measured at 25 °C and recalculated for the experimental temperature using the software. The precipitation reaction for norsethite can be described by:

$$Ba^{2+} + Mg^{2+} + 2CO_3^{2-} \leftrightarrow BaMg(CO_3)_2 \quad (1)$$

So the saturation state (Ω) of norsethite was determined as:

$$\Omega = \frac{(a_{Ba^{2+}})(a_{Mg^{2+}})(a_{CO_3^{2-}})^2}{K_{sp}} \quad (2)$$

where a stands for the activity of an aqueous species and $K_{sp} = 10^{-17.86}$ at 50 °C, $10^{-18.16}$ at 70 °C, and $10^{-19.85}$ at 130 °C (Lindner et al., 2018). And the saturation index (SI) of norsethite was expressed by

$$SI = \log(\Omega) \quad (3)$$

2.6. Isotope analysis

Magnesium isotope analysis was performed at the State Key Lab for Mineral Deposits Research, Nanjing University. Chemical purification of Mg from the solid and aqueous phases followed a well-established method in the lab (Hu et al., 2017; Bialik et al., 2018; Li et al., 2019). Recovery of Mg was >95% as determined by ICP-OES analyses of the Mg cut and matrix cut after ion exchange chromatography for every sample. The total procedural blank for the chemical procedure was <30 ng, which was negligible relative to the >40 μg of Mg that was processed for each sample. Magnesium isotope ratios were measured using a Thermo Scientific Neptune Plus multi-collector inductively coupled mass spectrometer (MC-ICP-MS). The instrument was operating in a low-mass-resolution mode, using a 100 ~μL/min self-aspirating nebulizer and a glass spray chamber. Instrument drift and mass bias was corrected using a standard-sample bracketing method using an in-house Mg solution (HPS909104) as the bracketing standard. The HPS909104 Mg solution has a δ^{26}Mg value of −0.66‰ relative to DSM3 (Li et al., 2012, 2015; Hu et al., 2017). The concentration of samples typically matched the in-house standard to better than ±10%. A 40 s on-peak acid blank was measured before each analysis. Each Mg isotope ratio measurement consisted of fifty 4-s integrations. Accuracy of Mg isotope analyses was monitored using pure Mg standards (Cambridge1 and DSM3), natural sample standards (IAPSO standard seawater, and USGS rock standard DST-2b), and a matrix-matching synthetic standard solution (mixture of $BaCl_2$ and in-house Mg standard HPS932001, 1:1 molar ratio). The natural sample standards and matrix-matching synthetic standards were treated as unknown samples together with samples from experiments by ion-exchange chromatography to assess the accuracy of the total chemical procedure. The external precision of the Mg isotope measurements was better than ±0.1‰ for δ^{26}Mg.

Magnesium isotope compositions are reported using the standard per mil (‰) notation of $\delta^{26}Mg$ and $\delta^{25}Mg$ for the $^{26}Mg/^{24}Mg$ and $^{25}Mg/^{24}Mg$ ratios relative to DSM3 Mg isotope standard, where

$$\delta^{x}Mg = \left[\left({}^{x}Mg/{}^{24}Mg_{sample}\right)/\left({}^{x}Mg/{}^{24}Mg_{DSM3}\right) - 1\right] \times 1000 \quad (4)$$

and Mg isotope fractionation between two phases A and B is expressed as:

$$\Delta^{x}Mg_{A-B} = \delta^{x}Mg_{A} - \delta^{x}Mg_{B} \approx 10^{3}\ln\alpha^{x/24}_{A-B} \quad (5)$$

where x = 25 or 26.

The error propagation function is applied for calculating the uncertainty in Mg isotope fractionation factors:

$$Err\Delta Mg_{A-B} = \left[(Err\delta Mg_{A})^{2} + (Err\delta Mg_{B})^{2}\right]^{1/2} \quad (6)$$

where $Err\Delta Mg_{A-B}$ refers to the error of the Mg isotope fractionation factor between phases A and B, and $Err\delta Mg_{A}$ and $Err\delta Mg_{B}$ stand for the errors of measurements of isotope compositions of phases A and B.

3. RESULTS

3.1. Mineralogy

The results of *in situ* XRD analyses, including representative raw Debye-rings data from the 2-D detector and the processed XRD diffraction patterns, are shown in Fig. 1 and Appendix Figs. S2 and S3. The lack of sharp diffraction peaks at the beginning of experiments was indicative of the presence of the AC. The AC persisted for about 1 hour at 70 °C (Situ70), 5.5 hours at 50 °C (Situ50) and 56 hours at 25 °C (Situ25), then characteristic peaks for norsethite began to appear. The first appearance of norsethite XRD peaks was broad and of low intensity, but the sharpness and intensity of the XRD peaks for norsethite increased, then plateaued afterwards. It is important to note that only diffraction peaks for norsethite were identified in all *in situ* experiments, and no diffraction peaks of other minerals were detected throughout the process of transformation from amorphous carbonate to norsethite.

The newly synthesized amorphous carbonate phase occurred as aggregates of homogeneous fine spheres with a size ranging between 50 and 200 nm (Fig. 2A). By contrast, the newly-formed norsethite at 50 °C and 70 °C exhibited euhedral to subhedral crystalline morphology (Fig. 2B, C), whereas products at 130 °C all occurred as spherical aggregates of euhedral to subhedral crystals (Fig. 2D).

Bulk powder XRD analysis also confirmed that the solid products of the exchange experiments were pure norsethite. The measured d(104) values for norsethite scattered around 3.009 Å, but d(104) did not show any notable correlations with reaction time or temperature in the different exchange experiments (Fig. 3A, Appendix TableS1). The Full Width at Half Maximum (FWHM, a parameter of peak sharpness) of the (104) peak, however, correlated with reaction time (Fig. 3B). Given the same reaction temperature, the FWHM of the (104) peak decreased with increasing reaction time.

3.2. Chemical composition of the AC and solutions

Based on ICP-OES analysis of 11 AC samples synthesized for different experiments, the AC contained 51.7–53.9 mol% Mg in its total divalent cation (Mg + Ba) budget, with an average value of 52.4 ± 1.4 mol% (2SD, n = 11; Appendix Table S2). This is very close to the stoichiometry of ideal norsethite (50 mol% Mg).

The chemical composition of the solutions are tabulated in Table 1. In experiments Ex70 and Ex50, the pH increased to around 8.7 during the early period of reaction and then gradually decreased with reaction time, while the pH remained relatively constant in experiment Ex130-2 (Fig. 4A, B, C) and it may indicate that the system had reached a steady state due to the higher reaction rate at higher temperatures. The solution alkalinity for all the experiments show drifting trends that are broadly similar to the solution pH (Fig. 4J, K, L). It should be noted that for experiment Ex70, low pH value (below 8) and alkalinity was measured for solutions sampled in the first one hour reaction time. For these aqueous solution samples, some tiny, but recognizable white cloudy solid material was identified at the bottom of centrifuge tubes. The solid material was inferred as newly precipitated Ba-Mg carbonates from the aqueous solution after sampling.

The measured solution Mg concentrations were around 80–100 mM during the whole reaction process (Fig. 4D, E, F). In contrast, the Ba concentration in experiments Ex70 and Ex50 were orders of magnitude lower than Mg concentration, and there was a slight increase in Ba^{2+} concentration in aqueous solution upon mixing the Ba-Mg AC with "solution D", which may be due to the dissolution of a fraction of Ba-Mg AC. It is important to note that the highest Ba concentration of the aqueous solution was measured to be 2.7 mM (Fig. 4G, H, I, Table 1), corresponding to <3% of Ba in the Ba-Mg AC. The Ba^{2+} contents in aqueous solution decreased rapidly during the transformation process of Ba-Mg AC to norsethite, and remained relatively constant and low values (<0.1 mM) after the transformation completed.

3.3. Isotope results

The "solution D" for isotope exchange experiments is isotopically enriched, and has a $\delta^{26}Mg$ value of −3.18‰ and $\delta^{25}Mg$ value of 82.93‰, which are 0.73‰ higher in $\delta^{26}Mg$ and 84.93‰ higher in $\delta^{25}Mg$ than the starting AC, respectively (Table 1). During transformation of the AC to crystalline norsethite, the $\delta^{26}Mg$ value of solid phase decreased while that of aqueous phase increased (Fig. 5A, B, C, D), which contributed to a −0.8‰ to −1.3‰ decline for $\Delta^{26}Mg_{solid\text{-}aq}$ within the first 12 hours. Following that, the $\delta^{26}Mg$ value for both phases remained relatively constant.

By contrast, the starting amorphous phase and solution had distinct $\delta^{25}Mg$ values and these values converged during exchange experiments (Fig. 5E, F, G, H). The changes in $\delta^{25}Mg$ values for both the solid and aqueous phases were

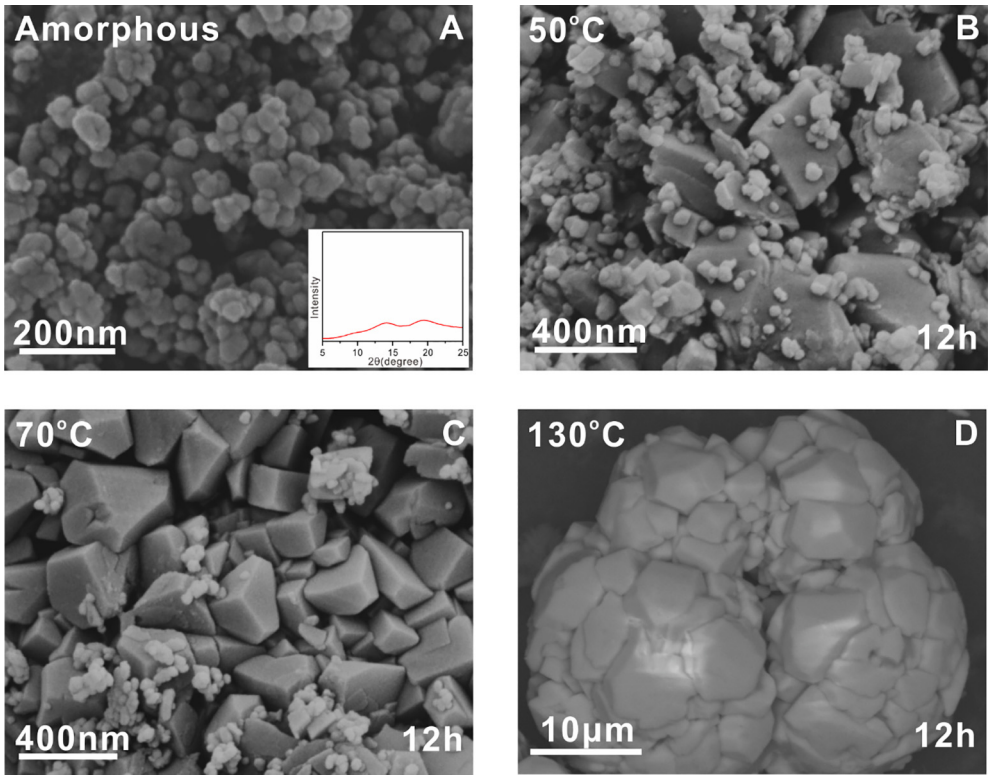

Fig. 2. (A) SEM image of amorphous carbonate and the XRD pattern of amorphous carbonate is embedded within it. (B) SEM image of norsethite in exchange experiments at 50 °C. (C) SEM image of norsethite in exchange experiments at 70 °C. (D) SEM image of norsethite in exchange experiments at 130 °C.

comparable, which corresponded to the ~1:1 molar ratio of Mg between the two phases. The changes in δ^{25}Mg values for both the solid and aqueous phases were fast within the first few reaction hours, and this was accompanied with the AC transformation to norsethite (Appendix Fig. S5).

It is important to note that in most exchange experiments, the δ^{25}Mg value of norsethite became greater than that of aqueous solution (Fig. 5E, F, G, H), producing positive $\Delta^{25}Mg_{solid\text{-}aq}$ values (Fig. 5M, N, O, P), while the $\Delta^{26}Mg_{solid\text{-}aq}$ values remained negative. In another words, the δ^{25}Mg values of the two phases of the system changed more rapidly than δ^{26}Mg values, and did not show an apparent mass dependent behavior (a more detailed analysis of this apparent non-mass dependent behavior is given in Section 4.2). This phenomenon was distinct in experiments 'Ex130-1', 'Ex70' and 'Ex50', but also occurred to some experimental products for experiment 'Ex130-2'. Such phenomenon had not been reported in any isotope exchange experiments in literature. We highlight that the exchange experiments were repeated, and in each experiment, separate parallel reaction vessels were sequentially sampled, and the differences in δ^{25}Mg and δ^{26}Mg values between solid and solution far exceed the external analytical precision (e.g., ±0.1‰ for δ^{26}Mg). Selected samples have been separately analyzed using a Nu 1700 MC-ICP-MS at the State Key Laboratory of Isotope Geochemistry, Guangzhou Institute of Geochemistry, Chinese Science Academy, and the results are highly consistent between the two labs (Appendix Table S5, Fig. S6). Therefore the observation was reproducible and we ruled out analytical artifact or experiment manipulation error as the cause of this phenomenon.

4. INTERPRETATION AND DISCUSSION

4.1. The reaction pathway of norsethite formation

4.1.1. Formation of the Ba-Mg AC

Norsethite formed via the transformation of amorphous carbonate precursor, which precipitation instantaneously upon mixing of the Mg^{2+}, Ba^{2+}, and CO_3^{2-} in aqueous solutions. The XRD patterns without any apparent diffraction peaks (Fig. 2A) but two broad humps at 2θ of ~14° and ~20° confirmed that this initial precipitate was poorly ordered and probably consisted of amorphous material, similar to many synthesized ACC (e.g., Levi-Kalisman et al., 2002; Faatz et al., 2004; Ajikumar et al., 2005; Rodriguez-Blanco et al., 2008), although it had been reported that anhydrous ACC or transient ACC with a nascent short-range order occurred in some biomineralization processes (Politi et al., 2006; Gong et al., 2012; Mass et al., 2017). Recently, Martignier et al. (2017) reported a kind of barium micropearls "ACC" with internal zonation, however, TEM data showed that this kind of ACC had no long-range structure so it was still an amorphous material. Zonation formed by the oscillations of relative content of

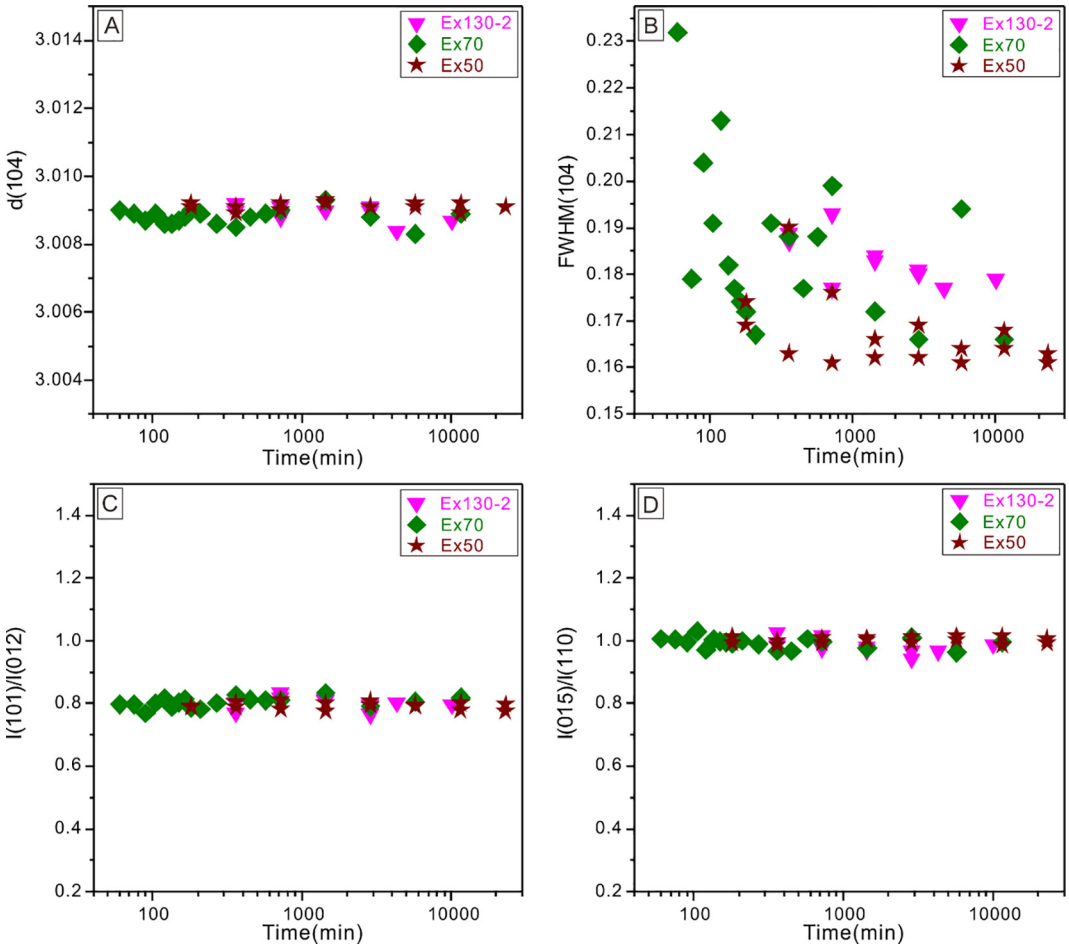

Fig. 3. Lattice parameters for norsethite in the exchange experiments. (A) norsethite d(104) versus reaction time,(B) FWHM of (104) for norsethite versus reaction time, (C) I(101)/I(012) versus reaction time, (D) I(015)/I(110) versus reaction time.

Ba and Ca and it may be related to specific biological process (Martignier et al., 2017), however, it was not the case for Ba-Mg AC.

The mineralogical characteristics of the Ba-Mg AC and the synthesized ACC reported in literature were remarkably similar in terms of the spherical morphology (e.g., Rodriguez-Blanco et al., 2012; Blue and Dove, 2015; Konrad et al., 2018) and apparent nano-porous structure with large surface area (Purgstaller et al., 2019). The particle size of the Ba-Mg AC was 50–200 nm and in our experiments, the initial aqueous Mg^{2+}:Ba^{2+}:(CO_3^{2-} + HCO_3^-) ratio was 2:1:2, and the (CO_3^{2-} + HCO_3^-) concentration was 0.2 M. In order to compare the Ba-Mg AC and ACC more systematically, we have conducted ACC synthesis experiment with initial Mg^{2+}:Ca^{2+}:(CO_3^{2-} + HCO_3^-) ratio of 2:1:2 (details described in Appendix) and the obtained ACC had a similar size with the Ba-Mg AC (Appendix Fig. S4). It should be noted that particle size of synthesized ACC in literature can vary from several nanometers to micrometers (Koga et al., 1998; Rodriguez-Blanco et al., 2014; Blue et al., 2017), and the particle size of the ACC may be related to the pH and temperature of aqueous solution (Faatz et al., 2004; Carino et al., 2017).

In contrast to the morphological similarity between Ba-Mg AC and ACC, the two AC display remarkable difference in cation ratios (i.e., mole ratio of Mg/(Mg + X), where X is a secondary alkaline element such as Ca or Ba). Notably, the Mg content of Ba-Mg AC in this study slightly exceeded 50 mol%, whereas most of the synthesized ACC contain less than 50 mol% Mg (Ajikumar et al., 2005; Lam et al., 2007; Jiang et al., 2010; Wang et al., 2011; Rodriguez-Blanco et al., 2012). Specifically, the Mg content of ACC synthesized in our experiments averaged at 44.5 ± 2.1 mol% (2SD, n = 11; Appendix Table S3), which was lower than that in Ba-Mg AC. Therefore it appears easier for Mg^{2+} to be incorporated into the Ba-Mg AC compared to the ACC. Although several studies reported formation of ACC that contains up to 100 mol% Mg (Radha et al., 2012; Yang et al., 2016; Purgstaller et al., 2019), it has been argued that the ACC containing more Mg than Ca is heterogeneous (Radha et al., 2012). It has been reported that the Mg content in ACC related to the chemistry of aqueous solution including Mg/Ca ratio (Loste et al., 2003; Wang et al., 2009; Hermans et al., 2011; Blue et al., 2017; Purgstaller et al., 2017), pH and CO_3^{2-} concentration (Blue and Dove, 2015) as well as presence of organic addi-

Table 1
Chemical composition data of solution and Mg isotope data of solution and solid phases in exchange experiments. Alkalinity: carbonate alkalinity of the solution; SI_{nor} : saturation index of norsethite calculated from Eq. (3).

Exp ID	Time (min)	Solution chemistry					Solution					Solid					Fractionation(solid-aq)			
		pH(25 °C)	Mg(mM)	Ba(mM)	Alkalinity(mM)	SI_{nor}	$\delta^{26/24}$Mg	2SD	$\delta^{25/24}$Mg	2SD	n(N)[a]	$\delta^{26/24}$Mg	2SD	$\delta^{25/24}$Mg	2SD	n(N)[a]	$\Delta^{26/24}$Mg	2SD	$\Delta^{25/24}$Mg	2SD
Test solution[b]							−2.89	0.07	−1.48	0.04	12(4)									
Test solution[c]							−2.93	0.11	−1.49	0.09	13(5)									
Solution D							−3.18	0.12	82.93	0.26	19(7)									
AC												−3.91	0.16	−2.00	0.09	17(8)				
Ex130-1	720						−2.64	0.04	35.23	0.02	2(1)	−4.14	0.10	39.47	0.03	2(1)	−1.50	0.11	4.24	0.04
	1440						−2.71	0.11	35.11	0.08	2(1)	−4.14	0.07	39.97	0.07	2(1)	−1.43	0.13	4.85	0.11
	2880						−2.48	0.00	36.09	0.78	2(1)	−4.21	0.06	39.97	0.03	2(1)	−1.74	0.06	3.88	0.78
	5760						−2.55	0.06	35.34	0.04	2(1)	−4.18	0.05	40.14	0.02	2(1)	−1.64	0.08	4.79	0.05
	11,520						−2.74	0.05	35.55	0.01	2(1)	−4.21	0.12	39.88	0.02	2(1)	−1.47	0.13	4.33	0.03
Ex130-2	360	7.80	79.76	0.05	2.92	0.97	−2.69	0.07	38.33	0.07	2(1)	−4.24	0.02	37.04	0.04	2(1)	−1.55	0.08	−1.28	0.08
	360	7.93	84.70	0.07	3.24	1.12	−2.64	0.10	42.02	0.01	2(1)	−4.40	0.04	36.02	0.07	4(1)	−1.75	0.11	−6.00	0.07
	720	7.87	77.76	0.03	1.95	0.20	−2.52	0.05	36.33	0.04	2(1)	−4.60	0.00	40.10	0.01	2(1)	−2.08	0.05	3.77	0.05
	720	7.87	86.41	0.04	2.92	0.87	−2.72	0.08	39.78	0.09	2(1)	−4.29	0.10	35.00	0.13	4(1)	−1.57	0.13	−4.79	0.16
	1440	7.97	85.16	0.03	2.27	0.45	−2.71	0.13	37.61	0.12	2(1)	−4.22	0.08	36.37	0.05	4(1)	−1.51	0.15	−1.24	0.13
	1440	7.96	81.28	0.06	2.60	0.71	−2.57	0.14	35.60	0.06	2(1)	−4.33	0.04	38.97	0.04	2(1)	−1.76	0.15	3.38	0.07
	2880	7.92	82.95	0.07	1.62	0.31	−2.65	0.06	37.88	0.03	2(1)	−4.30	0.02	36.56	0.01	2(1)	−1.65	0.07	−1.32	0.03
	2880	7.88	76.77	0.02	2.60	0.49	−2.65	0.19	39.07	0.09	2(1)	−4.41	0.04	36.85	0.03	2(1)	−1.76	0.19	−2.22	0.09
	4320	7.86	75.00	0.02	2.27	0.16	2.54	0.02	38.67	0.04	2(1)	−4.27	0.01	37.08	0.06	2(1)	−1.74	0.02	−1.59	0.07
	10,080	7.90	78.13	0.09	2.60	1.08	−2.71	0.06	35.67	0.05	2(1)	−4.33	0.09	41.74	0.00	4(1)	−1.63	0.11	6.06	0.05
Ex70	30	7.75	90.93	2.59	1.62	1.40	−3.04	0.01	64.97	0.04	2(1)	−3.85	0.14	9.77	0.06	4(1)	−0.82	0.14	−55.20	0.07
	45	7.77	95.07	1.98	2.60	1.82	−2.83	0.01	56.65	0.03	2(1)	−4.10	0.06	19.04	0.01	2(1)	−1.27	0.06	−37.61	0.03
	60	7.76	93.09	0.69	1.62	0.84	−2.62	0.05	43.20	0.01	2(1)	−3.99	0.05	27.52	0.02	2(1)	−1.37	0.07	−15.68	0.02
	75	8.74	98.89	0.02	2.92	0.90	−2.53	0.04	34.24	0.01	2(1)	−4.32	0.02	41.35	0.06	2(1)	−1.79	0.04	7.11	0.06
	90	8.64	91.67	0.03	2.60	1.01	−2.60	0.00	36.05	0.05	2(1)	−4.44	0.06	39.74	0.03	2(1)	−1.84	0.06	3.69	0.06
	105	8.66	91.03	0.02	3.24	1.09	−2.58	0.02	36.23	0.01	2(1)	−4.47	0.04	39.64	0.07	2(1)	−1.89	0.05	3.41	0.07
	120	8.11	90.90	0.05	3.24	0.89	−2.68	0.02	37.18	0.03	2(1)	−4.34	0.02	39.45	0.03	2(1)	−1.66	0.03	2.27	0.04
	135	8.1	90.56	0.03	2.92	0.47	−2.58	0.08	36.29	0.06	2(1)	−4.44	0.02	39.65	0.05	2(1)	−1.87	0.08	336	0.08
	150	8.67	93.78	0.02	2.60	0.84	−2.63	0.08	35.67	0.05	2(1)	−4.40	0.14	40.61	0.02	2(1)	−1.77	0.16	4.93	0.05
	165	8.64	96.84	0.01	2.27	0.43	−2.62	0.02	36.07	0.03	2(1)	−4.36	0.05	41.04	0.00	2(1)	−1.74	0.05	5.06	0.03
	180	8.72	97.04	0.01	3.89	1.04	−2.46	0.04	34.42	0.03	2(1)	−4.46	0.01	42.53	0.03	2(1)	−2.00	0.04	8.11	0.05
	210	8.21	102.18	0.02	3.24	0.58	−2.56	0.04	34.41	0.07	2(1)	−4.32	0.07	41.89	0.07	2(1)	−1.76	0.08	7.48	0.09
	270	8.53	94.44	0.02	2.92	0.88	−2.67	0.05	36.81	0.03	2(1)	−4.33	0.03	38.84	0.06	2(1)	−1.66	0.05	2.03	0.07
	360	8.27	98.46	0.03	2.92	0.75	−2.62	0.00	35.56	0.02	2(1)	−4.39	0.04	40.17	0.03	2(1)	−1.77	0.04	4.60	0.04
	450	8.41	103.84	0.04	2.92	0.92	−2.57	0.05	35.90	0.03	2(1)	−4.36	0.05	39.75	0.06	2(1)	−1.79	0.07	3.85	0.07
	570	8.43	89.32	0.03	3.24	0.98	−2.65	0.02	37.68	0.00	2(1)	−4.41	0.02	39.08	0.04	2(1)	−1.76	0.03	1.40	0.04
	720	8.31	96.52	0.04	3.57	1.08	−2.73	0.02	38.70	0.02	2(1)	−4.22	0.00	37.19	0.00	2(1)	−1.49	0.02	−1.52	0.02
	1440	8.11	107.02	0.05	2.92	0.74	−2.63	0.07	37.50	0.06	2(1)	−4.27	0.01	38.78	0.03	2(1)	−1.64	0.07	1.28	0.07
	2880	7.92	98.12	0.04	1.62	−0.26	−2.58	0.00	36.28	0.05	2(1)	−4.41	0.08	40.44	0.00	2(1)	−1.83	0.08	4.17	0.05
	5760	7.87	92.52	0.06	1.30	−0.40	−2.72	0.07	37.89	0.05	2(1)	−4.21	0.07	37.12	0.01	2(1)	−1.49	0.10	−0.77	0.05
	11,520	7.73	102.89	0.08	2.60	0.39	−2.60	0.03	37.68	0.04	2(1)	−4.32	0.02	38.67	0.02	2(1)	−1.72	0.04	0.99	0.05

Ex50	180	7.92	77.77	0.51	3.57	1.81	−2.61	0.03	46.15	0.01	2(1)	−4.49	0.16	27.63	0.12	2(1)	−1.88	0.17	−18.51	0.12
	180	7.86	76.55	0.44	2.92	1.47	−2.60	0.13	44.93	0.06	2(1)	−4.50	0.18	31.17	0.07	2(1)	−1.90	0.23	−13.77	0.09
	360	8.48	78.88	0.01	5.19	1.30	−2.65	0.14	35.97	0.07	2(1)	−4.48	0.03	38.29	0.02	2(1)	−1.84	0.14	2.32	0.07
	360	8.61	79.14	0.00	4.87	0.50	−2.52	0.02	37.50	0.01	3(1)	−4.62	0.02	37.55	0.03	2(1)	−2.10	0.03	0.05	0.04
	720	8.44	80.26	0.01	4.54	1.21	−2.53	0.02	34.19	0.11	3(1)	−4.53	0.01	39.10	0.07	2(1)	−2.00	0.02	4.91	0.13
	720	8.33	77.78	0.01	4.22	0.86	−2.49	0.03	35.44	0.04	3(1)	−4.46	0.03	36.28	0.02	2(1)	−1.97	0.05	0.84	0.04
	1440	8.24	77.44	0.01	3.89	0.78	−2.51	0.05	34.62	0.05	3(1)	−4.53	0.09	39.28	0.01	3(1)	−2.02	0.11	4.66	0.05
	1440	8.12	78.38	0.02	2.60	0.40	−2.63	0.04	32.45	0.05	3(1)	−4.37	0.14	37.62	0.02	3(1)	−1.74	0.14	5.17	0.06
	2880	8.03	74.07	0.02	2.60	0.23	−2.52	0.08	35.25	0.03	3(1)	−4.63	0.05	40.18	0.01	3(1)	−2.11	0.10	4.93	0.03
	2880	8.12	75.61	0.04	2.27	0.49	−2.47	0.07	36.60	0.05	3(1)	−4.62	0.11	37.08	0.04	3(1)	−2.15	0.13	0.48	0.06
	5760	7.96	78.90	0.02	2.92	0.15	−2.55	0.03	36.26	0.03	3(1)	−4.56	0.06	37.07	0.04	3(1)	−2.01	0.07	0.81	0.05
	5760	7.98	80.89	0.01	2.60	0.05	−2.48	0.07	34.48	0.04	3(1)	−4.58	0.06	40.40	0.04	3(1)	−2.10	0.09	5.93	0.06
	11,520	7.93	79.02	0.02	1.62	−0.35	−2.47	0.03	35.76	0.05	3(1)	−4.62	0.07	41.11	0.04	3(1)	−2.15	0.08	5.34	0.06
	11,520	7.9	76.36	0.02	2.60	0.12	−2.42	0.05	33.96	0.05	3(1)	−4.71	0.02	40.99	0.02	3(1)	−2.29	0.05	7.03	0.06
	23,040	7.83	78.54	0.08	1.95	0.31	−2.49	0.07	36.65	0.01	3(1)	−4.48	0.04	37.99	0.04	3(1)	−1.99	0.08	1.33	0.04
	23,040	7.86	79.08	0.07	2.27	0.44	−2.55	0.01	34.61	0.02	3(1)	−4.57	0.08	39.07	0.06	3(1)	−2.03	0.08	4.46	0.06

[a] n denotes the total number of isotope analysis, N denotes the number of replicate.
[b] Test solution contains 0.8 μmol of Mg (HPS932001, $\delta^{26}Mg = -2.93‰$) and 0.8 μmol of $BaCl_2$.
[c] Test solution contains 0.4 μmol of Mg (HPS932001, $\delta^{26}Mg = -2.93‰$) and 0.4 μmol of $BaCl_2$.

tives (Aizenberg et al., 2002; Wang et al., 2009). It is possible that some of these factors had also affected the Ba-Mg AC in our study.

4.1.2. Transformation of the Ba-Mg AC to norsethite

The Ba-Mg AC transformed to crystalline nano-norsethite in all experiments. *In situ* XRD analysis revealed that the transformation took about 1 hour at 70 °C (Fig. 1), 5.5 hours at 50 °C (Appendix Fig. S2) and 56 hours at 25 °C (Appendix Fig. S3), which was consistent with Pimentel and Pina (2014, 2016) who reported that it takes 24–72 h for transformation of amorphous Ba-Mg carbonate to crystalline norsethite at room temperature. Therefore, temperature is a key controlling factor for the rate of Ba-Mg AC transformation and it is the same for ACC transformation, which proceeds at a faster rate under a higher temperature (Long et al., 2011; Rodriguez-Blanco et al., 2011). Meanwhile, a number of studies reported that the synthesized ACC only lasted a short time (i.e., a few minutes) at room temperature before its transformation (e.g., Rodriguez-Blanco et al., 2012, 2014; Wang et al., 2012; Purgstaller et al., 2016, 2017), therefore, the Ba-Mg AC in our study appeared to have a higher stability compared to the ACC. The most notable difference between the Ba-Mg AC and ACC was the Mg content and it was reported that Mg played an important positive role in stabilizing ACC (Aizenberg et al., 2002; Loste et al., 2003; Lam et al., 2007; Jiang et al., 2010; Singer et al., 2012; Blue et al., 2017; Purgstaller et al., 2017). However, other parameters such as the Mg^{2+} concentration in the aqueous solution (Konrad et al., 2018) and the particle size (Nudelman et al., 2010; Zou et al., 2015) also have significant influence on the stability of ACC. More work is needed to compare the stability of these two types of amorphous carbonates systematically.

In this study, no intermediate phases was observed during transformation of amorphous carbonate to norsethite (Fig. 1, Appendix Figs. S2, S3 and S5). This is different from the norsethite synthesis experiments by Pimentel and Pina (2014, 2016), who reported that transformation of amorphous carbonate to norsethite was accompanied with precipitation and dissolution of intermediate minerals including northupite, eitelite, hydromagnesite and witherite. The different reaction pathways may result from the different conditions used between these experiments. Notably, in this study, the molar ratio of $(Mg + Ba):CO_3^{2-}$ in the reactant was above one, whereas in the study of Pimentel and Pina (2014, 2016), the $(Mg + Ba):CO_3^{2-}$ ratios for reactants were below one. Studies on ACC transformation have shown that the mineralogy of intermediate and final minerals are dependent on chemical conditions of the aqueous solution (e.g., Lam et al., 2007; Rodriguez-Blanco et al., 2012; Blue et al., 2017; Purgstaller et al., 2017). The saturation indexes (SI) of magnesite, northupite, eitelite and witherite were all negative for the exchange experiments (Appendix Table S4), corroborating the absence of these minerals during Ba-Mg AC transformation. It is notable that the calculated SI of hydromagnesite in experiments at 50 °C and 70 °C were slightly positive, but given the apparent inconsistency in solubility of hydromagnesite reported by different authors

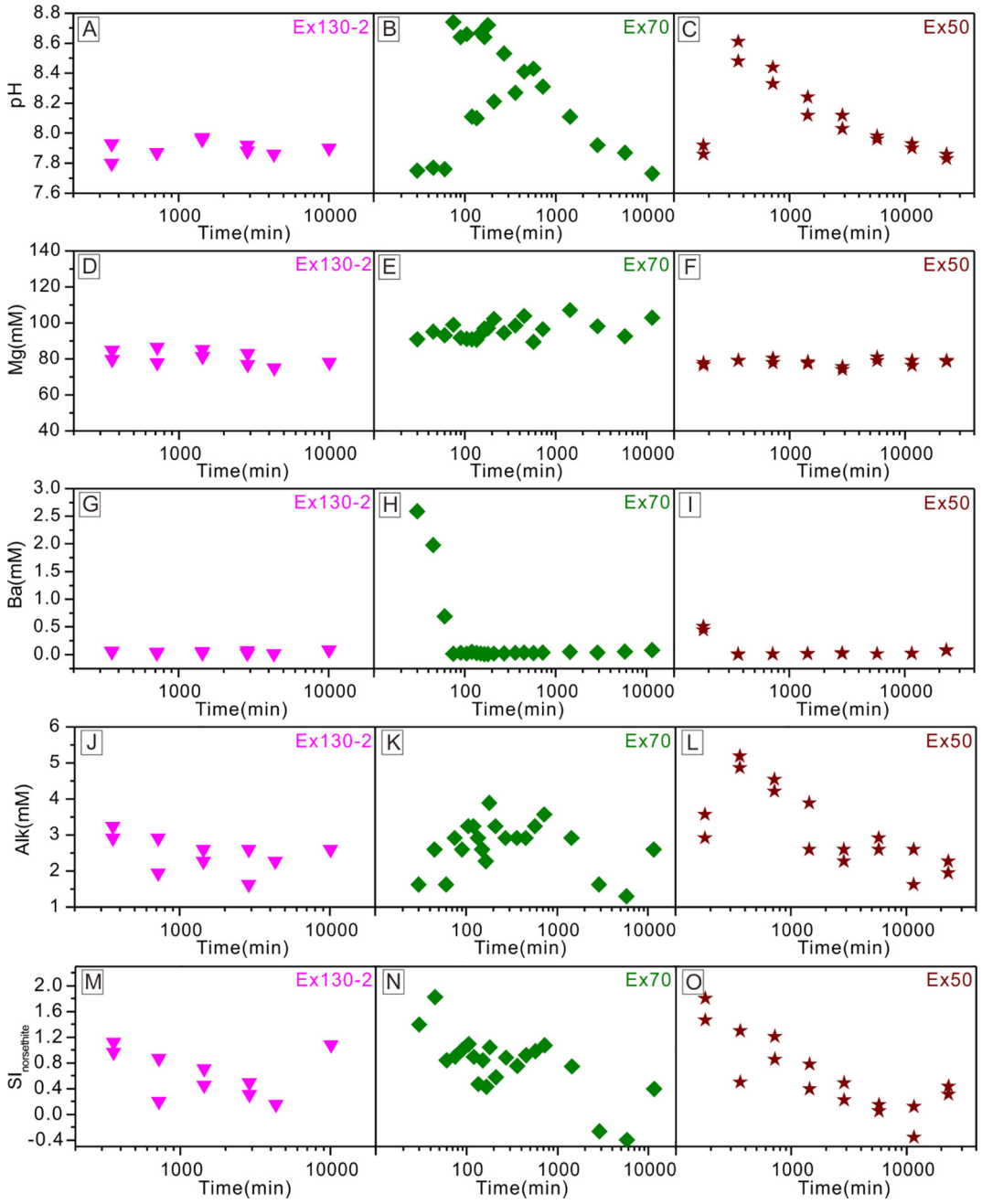

Fig. 4. Temporal chemical evolution of reactive solution with reaction time in exchange experiments: Ex130-2, Ex70 and Ex50. Plots of pH values (measured at 25 °C) versus reaction time (A, B, C). Plots of Mg^{2+} concentration versus reaction time (D, E, F). Plots of Ba^{2+} concentration versus reaction time (G, H, I). Plots of carbonate alkalinity versus reaction time (J, K, L). Plots of $SI_{norsethite}$ versus reaction time (M, N, O).

(Königsberger et al., 1999; Cheng and Li, 2010; Xiong, 2011; Gautier et al., 2014), the slightly positive SI for hydromagnesite in our experiments should be evaluated with caution. Therefore, experimental observations and theoretical calculations consistently show that transformation from Ba-Mg AC to norsethite can proceed without intermediate mineral phases.

Since completion of transformation of Ba-Mg AC to norsethite, the slurry remained a simple binary system that only consisted of pure norsethite and aqueous solution. For minerals with dolomite-like structures, ordering of cations is an important parameter. In general, the intensity ratio of peak (015) and peak (110) is commonly used to constrain the degree of cation ordering for dolomite-type minerals (Schultzguttler, 1986; Li et al., 2015). According to Pimentel and Pina (2014), the I(101)/I(012) can also be used to evaluate the degree of Ba-Mg cation ordering. In all exchange experiments, the ratios of I(015)/I(110) and I

(101)/(012) showed little change after the formation of crystalline norsethite, irrespective of reaction time (Fig. 3C, D), which suggest that the norsethite was initially formed with high degree of Ba-Mg cation ordering. In other words, the changes in crystallinity and cation ordering of norsethite were decoupled during its recrystallization. And these results are consistent with the study of Pimentel and Pina (2016). This is different from the phenomenon in dolomite synthesis experiments, which always started with formation of poorly ordered protodolomite, and the degree of Ca-Mg cation ordering increased gradually during dolomite synthesis experiments (e.g., Katz and Matthews, 1977; Sibley et al., 1987; Kaczmarek and Sibley, 2011; Li et al., 2015; Montes-Hernandez et al., 2016; Kaczmarek and Thornton, 2017; Kell-Duivestein et al., 2019)

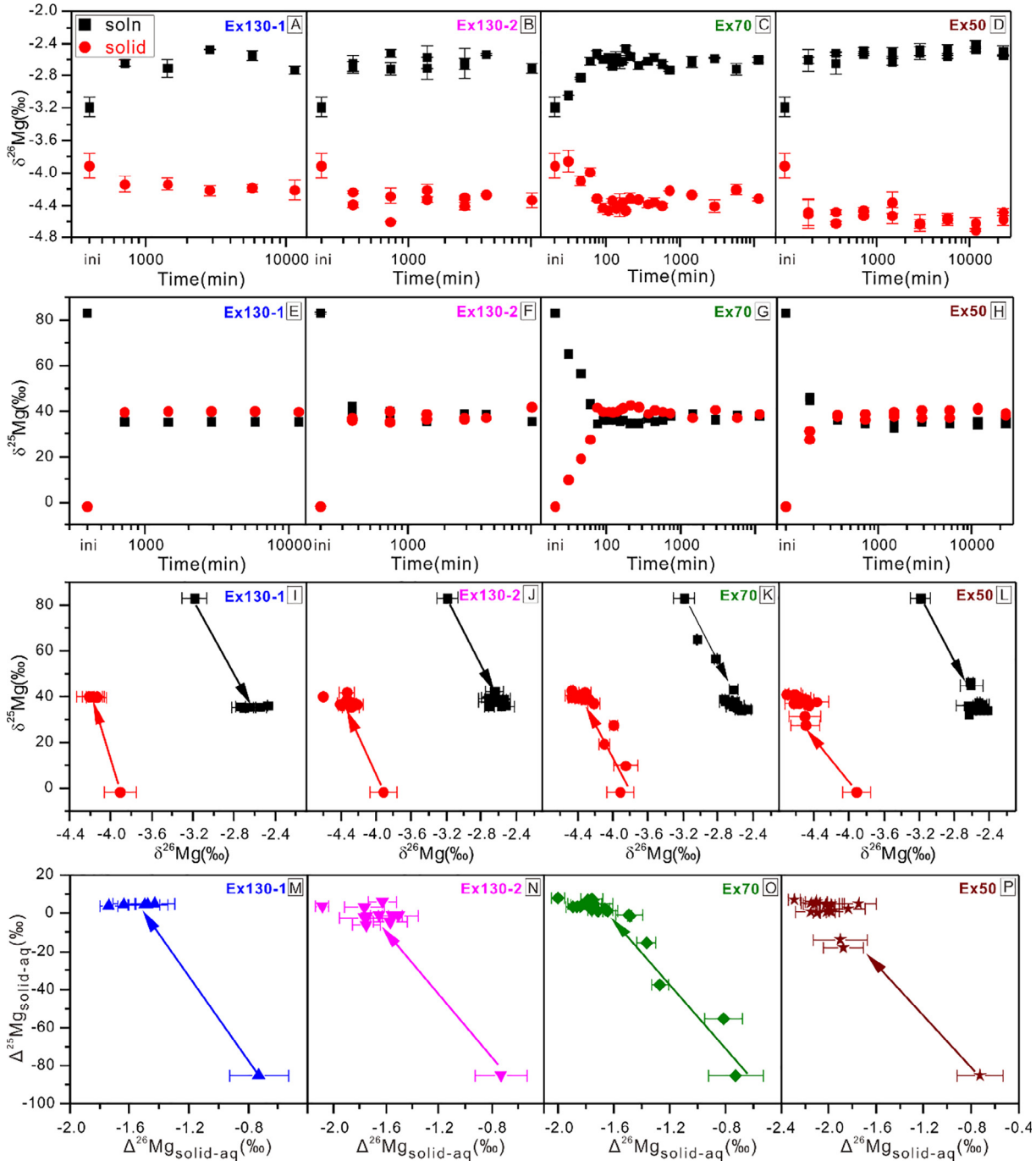

Fig. 5. Plots of the evolution of Mg isotopes in exchange experiments. Plots of δ^{26}Mg values versus reaction time (A, B, C, D). Plots of δ^{25}Mg values versus reaction time (E, F, G, H). Plots of δ^{26}Mg versus δ^{25}Mg values (I, J, K, L). Plots of $\Delta^{25}Mg_{solid\text{-}aq}$ versus $\Delta^{26}Mg_{solid\text{-}aq}$ fractionations values (M, N, O, P). The arrow shows the direction of change for δ^{26}Mg, δ^{25}Mg, $\Delta^{25}Mg_{solid\text{-}aq}$ and $\Delta^{26}Mg_{solid\text{-}aq}$.

4.2. Exchange of Mg isotopes during transformation of AC to norsethite

Two mechanisms have been proposed for explaining transformation of AC to crystalline carbonates, including a solid-state transition mechanism and a coupled dissolution-reprecipitation mechanism. The ^{43}Ca-^{25}Mg tracer study of ACC transformation by Giuffre et al. (2015) provided a strong argument favoring the latter mechanism, however, there was a caveat in the rational of the study, that it assumed no exchange between the ACC and surrounding solutions prior to ACC transformation, which has not been proven. The isotope exchange between crystalline minerals and solution had been widely recognized (Li et al., 2011, 2014; Mavromatis et al., 2016, 2017a; Oelkers et al., 2019; Skierszkan et al., 2019). Additionally, the large surface area of AC (Purgstaller et al., 2019) could potentially facilitate efficient isotopic exchange with the aqueous solution (Frierdich et al., 2019; Zheng et al., 2019). Moreover, unlike the highly ordered and packed crystalline minerals, amorphous phases are hydrated, loose, and porous (Goodwin et al., 2010), which could facilitate diffusion that is much faster than solid-state diffusion in crystalline minerals (Stipp et al., 1998; Jensen et al., 2018), further increasing the degree of isotope exchange. Therefore, the isotopic tracer study by Giuffre et al. (2015) is not conclusive about the actual mechanism of AC transformation, as the possibility of isotope exchange between ACC and solution prior to solid-state transition cannot be rigorously ruled out based on the experimental data of Giuffre et al. (2015).

In this study, we also used a ^{25}Mg-enriched tracer to study the cation exchange during the transformation of AC in aqueous solution, similar to Giuffre et al. (2015), but we took a step further and performed high precision measurements on both $^{26/24}Mg$ and $^{25/24}Mg$ ratios, following the concept of the "three-isotope method" (Matthews et al., 1983; Li et al., 2011; Frierdich et al., 2014b; Zheng et al., 2016). Experiments show that the fast transformation of AC to norsethite was accompanied with rapid and systematic changes in Mg isotope compositions in solid and aqueous phases, where $\delta^{26}Mg$ values of the two phases diverged but $\delta^{25}Mg$ values of the two phases converged (Fig. 5). This reflects isotope fractionation in association with cation exchange between the solid and aqueous phases during the transformation of AC. Except for some photochemical or organo-chemical reactions of certain elements (e.g., S, Thiemens, 1999; Farquhar et al., 2000; Ono et al., 2003; Hg, Bergquist and Blum, 2007; Sherman et al., 2010; Point et al., 2011), most of isotopes in terrestrial conditions demonstrate mass-dependent behavior (Johnson et al., 2004). According to the mass dependent fractionation law of isotopes, one would expect the experimental system to evolve towards isotopic equilibrium, where isotope fractionation factors are also mass dependent, e.g., $\Delta^{25}Mg_{min\text{-}aq} \approx 0.5 \times \Delta^{26}Mg_{min\text{-}aq}$ (for more precise description of this relation, see Young et al., 2002). This explains the convergence of $\delta^{25}Mg$ values of the two phases during exchange experiments (Fig. 5E, F, G, H).

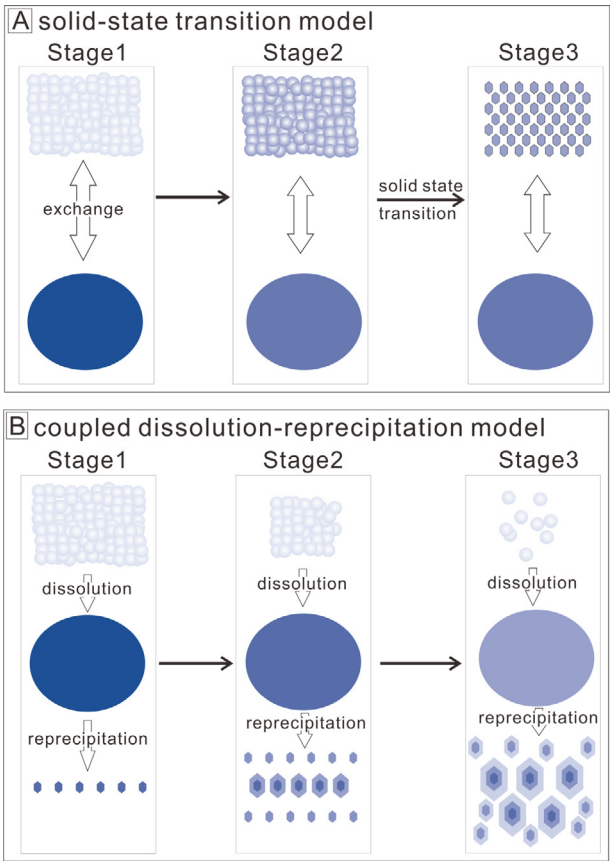

Fig. 6. Conceptual models of AC transformation. (A) The solid-state transition model. (B) The coupled dissolution-reprecipitation model. The spheres in represent the amorphous carbonate precursor, the hexagons represent the norsethite crystals, and the ellipses represent solution. The darkness of color illustrates the enrichment of ^{25}Mg tracers.

It is remarkable, however, the $\delta^{25}Mg$ values of the two phases in the exchange experiments not only converged, but overshot and crossed over the presumed equilibrium values (Fig. 5E, F, G, H). It resulted in the positive $\Delta^{25}Mg_{min\text{-}aq}$ values that were much greater than the values of $0.5 \times \Delta^{26}Mg_{min\text{-}aq}$ for many cases (Fig. 5M, N, O, P). As a result, while the $\delta^{26}Mg$ of aqueous solution after reaction was higher than that of the norsethite, $\delta^{25}Mg$ of aqueous solution after reaction was lower than that of the norsethite. This is an apparent non-mass dependent behavior and is unexpected in conventional practices of "three isotope method". Li et al. (2015) proposed that the degree of isotope exchange (F) in "three isotope" exchange experiments can be calculated using an equation:

$$F = (\Delta^{25}Mg_t - \Delta^{25}Mg_i)/(\Delta^{25}Mg_e - \Delta^{25}Mg_i) \quad (7)$$

where $\Delta^{25}Mg_t$ refers to the difference in $\delta^{25}Mg$ values between the solid and aqueous pair at a given time t ($\delta^{25}Mg_{solid}$-$\delta^{25}Mg_{aq}$, or $\Delta^{25}Mg_{solid\text{-}aq}$), and $\Delta^{25}Mg_i$ and $\Delta^{25}Mg_e$ stand for the initial and equilibrium $\Delta^{25}Mg_{solid\text{-}aq}$ values, respectively. Using this equation, the degrees of Mg isotope exchange are calculated to be 100%–110% for

the experiments, but a > 100% isotope exchange is unreasonable. The slight increase in aqueous Ba concentration in exchange experiments implied that a small fraction (<3%) of Ba-Mg AC was dissolved into the solution, however, the influence of such process was insignificant, as evidence by the large contrast in and δ^{25}Mg values between Ba-Mg AC and aqueous solution at the beginning of exchange experiments (Fig. 5E, F, G, H). So the unexpected non-mass dependent behavior of Mg isotopes in exchange experiments suggests that some specific process occurred during AC transformation, thus offering an opportunity to evaluate the mechanisms of isotope exchange during the transformation AC to crystalline norsethite.

In order to interpret Mg isotope data from the exchange experiments, we consider two extreme scenarios of AC transformation to norsethite according to the existing theories (Fig. 6) and model the isotopic response (in both δ^{26}Mg and δ^{25}Mg) of solid and aqueous solutions during the AC transformation processes. In scenario 1 (Fig. 6A), we assume that isotope exchange and fractionation took place between the amorphous phase and aqueous solution prior to solid-state transition of AC, and isotope diffusion within the amorphous carbonate outpaced the isotope exchange between the amorphous carbonate and aqueous solution, therefore both solid and aqueous phases were isotopically homogeneous. When tranformation happened, isotopic exchange between the solid and aqueous phases was frozen. In scenario 2 (Fig. 6B), we assume that there was no direct surficial and diffusional isotope exchange between aqueous solution and AC, instead isotopic exchange between the solid and aqueous phases occurred via dissolution of the amorphous carbonate, when the isotopes from the dissolved amorphous carbonates were released and homogenized with the existing aqueous solution. At the same time, an equal amount of material was precipitated from the aqueous solution as norsethite, therefore there was no net mass transfer between the solid and aqueous phases. These two extreme scenarios represent the solid-state transition mechanism (Politi et al., 2008) and the dissolution-reprecipitation mechanism (Giuffre et al., 2015), respectively.

The Mg isotope behaviors in these two scenarios can be modeled using numeric approaches similar to those that have been detailed by Cao and Bao (2017). Briefly, in model A (Fig. 6A) that describes scenario 1, we have

$$\frac{dMg_A}{dt} = J_{SA} - J_{AS} = 0 \tag{8a}$$

$$\frac{dMg_S}{dt} = J_{AS} - J_{SA} = 0 \tag{8b}$$

$$\frac{d^{24}Mg_A}{dt} = -\frac{d^{24}Mg_S}{dt} = \left(J_{SA}\frac{1}{1+{}^{25}\alpha\,{}^{25}R_S+{}^{26}\alpha\,{}^{26}R_S} - J_{AS}\frac{1}{1+{}^{26}R_A+{}^{26}R_A}\right) \tag{9a}$$

$$\frac{d^{x}Mg_A}{dt} = -\frac{d^{x}Mg_S}{dt} = \left(J_{SA}\frac{{}^{x}R_S\,{}^{x}\alpha}{1+{}^{25}\alpha\,{}^{25}R_S+{}^{26}\alpha\,{}^{26}R_S} - J_{AS}\frac{{}^{x}R_A}{1+{}^{26}R_A+{}^{26}R_A}\right) \tag{9b}$$

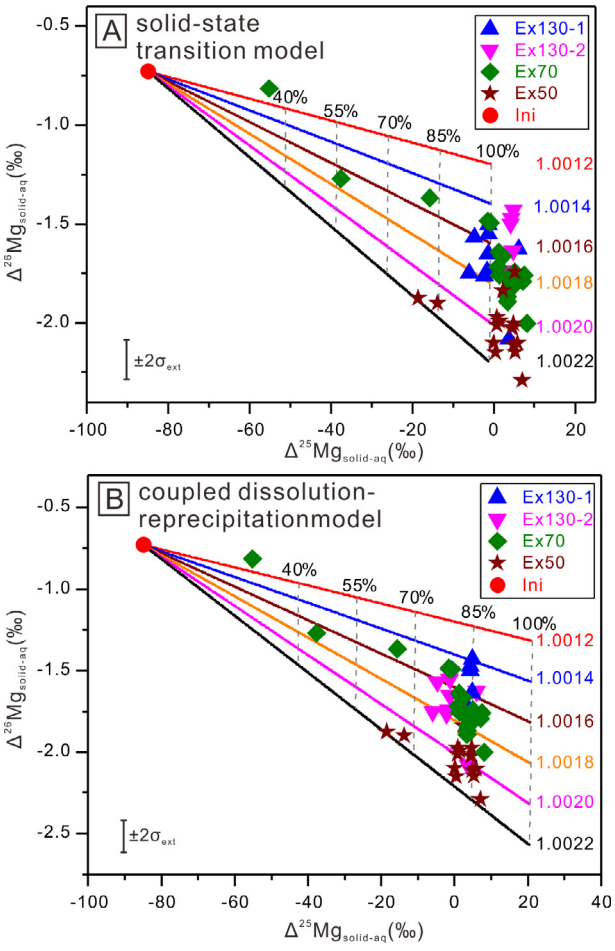

Fig. 7. Comparison of the results of numeric modeling and the experimental data. The solid lines represent the modeling results using different Mg isotope fractionation factors ($^{26}\alpha$) and the solid dots represent the experimental data (Table 1).

Eqs. (8a) and (8b) define that there is no net mass transfer between the solid (S) and aqueous (A) phases; J_{SA} and J_{AS} refer to the diffusional fluxes from S to A and A to S, respectively. Eqs. (9a) and (9b) define that the isotope exchange and fractionation between the two phases only occur during the exchange between the amorphous phase and aqueous solution, where $^{25}\alpha$ and $^{26}\alpha$ ($^{25}\alpha = {}^{26}\alpha^{0.52}$) denote the apparent fractionation factors of $^{25}Mg/^{24}Mg$ and $^{26}Mg/^{24}Mg$ during diffusion, respectively; $^{x}R_S$ ($=^{x}Mg_S/^{24}Mg_S$) and $^{x}R_A$ ($=^{x}Mg_A/^{24}Mg_A$) are Mg isotope ratios for S and A, x = 25 or 26.

In model B (Fig. 6B) that describes scenario 2, we have

$$\frac{dMg_A}{dt} = -J_{AS} \tag{10a}$$

$$\frac{dMg_S}{dt} = J_{AS} - J_{SC} = 0 \tag{10b}$$

$$\frac{dMg_C}{dt} = J_{SC} \tag{10c}$$

$$\frac{d^{24}Mg_S}{dt} = J_{AS}\frac{1}{1 + {}^{25}R_A + {}^{26}R_A} - J_{SC}\frac{1}{1 + {}^{25}\alpha^{25}R_S + {}^{26}\alpha^{26}R_S} \quad (11a)$$

$$\frac{d^{x}Mg_S}{dt} = J_{AS}\frac{{}^{x}R_A}{1 + {}^{25}R_A + {}^{26}R_A} - J_{SC}\frac{{}^{x}R_s{}^{x}\alpha}{1 + {}^{25}\alpha^{25}R_s + {}^{26}\alpha^{26}R_s} \quad (11b)$$

$$\frac{d^{24}Mg_C}{dt} = J_{SC}\frac{1}{1 + {}^{25}\alpha^{25}R_S + {}^{26}\alpha^{26}R_S} \quad (12a)$$

$$\frac{d^{x}Mg_C}{dt} = J_{SC}\frac{{}^{x}R_S{}^{x}\alpha}{1 + {}^{25}\alpha^{25}R_S + {}^{26}\alpha^{26}R_S} \quad (12b)$$

Eqs. (10a)-(10c) define that there is no net mass transfer between the solid and aqueous phases. The solid phase includes the amorphous carbonate (A) and crystalline norsethite (C). And the mass of Mg in aqueous solution (S) remains constant during the reaction. J_{AS} and J_{SC} refer to the dissolution flux from A to S and reprecipitation flux from S to C, respectively. Eqs. (11a), (11b), (12a) and (12b) define that dissolution of the amorphous carbonate (A) is congruent and is not associated with Mg isotope fractionation, but precipitation of crystalline norsethite (C) is associated with Mg isotope fractionation factors of $^{25}\alpha$ and $^{26}\alpha$ ($^{25}\alpha = {}^{26}\alpha^{0.52}$; Young et al., 2002). $^{x}R_S$ ($=^{x}Mg_S/^{24}Mg_S$), $^{x}R_S$ ($=^{x}Mg_S/^{24}Mg_S$), $^{x}R_A$ ($=^{x}Mg_A/^{24}Mg_A$) and $^{x}R_C$($=^{x}Mg_C/^{24}Mg_C$) are Mg isotope ratios for S, C and A, respectively.

In the two models, we set the solution phase (S) and amorphous phase (A) of initial system to contain equal amount of Mg, but with different Mg isotope compositions to mimic the exchange experiments. The initial aqueous solution phase (S) is set to have δ^{26}Mg value of −3.18‰ and δ^{25}Mg value of 82.93‰, respectively, whereas the initial amorphous phase (A) has δ^{26}Mg value of −3.91‰ and δ^{25}Mg value of −2.00‰, respectively (Table 1). We then allow the reaction between the two phases to proceed according to a solid-state-transition scenario (Model A, Fig. 6A) and a coupled dissolution-reprecipitation scenario (Model B, Fig. 6B), assuming different instantaneous mass-dependent Mg isotope fractionation factors (Fig. 7). Then we can numerically solve the models and obtain δ^{25}Mg and δ^{26}Mg values of each phase at any given degree of exchange between the amorphous phase and aqueous solution. The detailed modeling results are given in Appendix and plotted in a space of $\Delta^{25}Mg_{solid\text{-}aq}$ versus $\Delta^{26}Mg_{solid\text{-}aq}$ for the two models (Fig. 7). The experimental results are also plotted in Fig. 7 for comparison.

Both models predict that with increasing isotope exchange between the solid and aqueous phases, the $\Delta^{25}Mg_{solid\text{-}aq}$ value increases while $\Delta^{26}Mg_{solid\text{-}aq}$ value decreases, a relationship that is confirmed by the results of exchange experiments. However, model A predicts that the maximum $\Delta^{25}Mg_{solid\text{-}aq}$ is about $0.5 \times \Delta^{26}Mg_{solid\text{-}aq}$ at 100% isotope exchange, which could not exceed 0 (Fig. 7A). By contrast, model B predicts positive $\Delta^{25}Mg_{solid\text{-}aq}$ values as high as 20‰ for complete exchange between amorphous phase and aqueous solution (Fig. 7B). Obviously, results of model A are not consistent with the experimental data, thus solid-state transition cannot be the mechanism of AC transformation to norsethite; by contrast, model B better describes the experimental data (i.e., the positive and apparently non-mass dependent $\Delta^{25}Mg_{solid\text{-}aq}$ values after exchange experiments), thus providing an unequivocal proof for the dissolution-reprecipitation pathway as the AC transformation mechanism. The positive $\Delta^{25}Mg_{solid\text{-}aq}$ value was originated from the isotopic heterogeneity within individual norsethite crystals grew in aqueous solution that had dynamically changing Mg isotope compositions during exchange experiments. Therefore, combination of the experiments and modeling, we conclude that coupled dissolution-reprecipitation is the key mechanism for transformation of amorphous phase to crystalline carbonate, at least for the Ba-Mg-carbonate system.

4.3. Implications

4.3.1. Interpretations of metal stable isotope records of carbonates

There are growing interests in using Mg and Ca isotopes in natural carbonate archives to study the seawater chemistry and global Mg-Ca cycles in geological times (e.g., Farkaš et al., 2007; Müller et al., 2011; Du Vivier et al., 2015; Higgins and Schrag, 2015; Li et al., 2015; Lau et al., 2017; Wang et al., 2019). It has been realized that multiple issues, including variability in the sedimentary background of the carbonates (Geske et al., 2015a; Bialik et al., 2018), and post-depositional processes such as diagenesis (Immenhauser et al., 2005; Steuber and Buhl, 2006; Fantle and Higgins, 2014; Mavromatis et al., 2014; Blättler et al., 2015; Geske et al., 2015b; Huang et al., 2015; Chanda and Fantle, 2017; Higgins et al., 2018; Li et al., 2019), burial metamorphism (Geske et al., 2012; Azmy et al., 2013; Hu et al., 2017), as well as hydrothermal alteration (Lavoie et al., 2014; Walter et al., 2015; Riechelmann et al., 2016, 2018; Hu et al., 2019), need to be identified and isolated before interpretations of the Mg and Ca isotope proxy data from carbonate sediments. Given that the carbonates have been screened for these issues, the common reaction pathway involving amorphous precursor for precipitation of carbonate minerals arises further questions about how can the Mg and Ca isotope signatures in carbonate sediments be appropriately interpreted. Mavromatis et al. (2017b) have shown that the behavior of Mg isotopes differ between processes of direct calcite precipitation and Mg-ACC precipitation, which could bring complexities to Mg isotope studies of carbonates if calcite can be transformed from ACC via solid-state transition. Additionally, AC can be produced and stabilized during various biological process in natural systems (Aizenberg et al., 1996, 2002, 2003; Weiss et al., 2002; Briones et al., 2008; Al-Sawalmih et al., 2009), yet the isotopic effect of biologically-mediated AC transformation is little known. However, our study has shown that the AC transforms to carbonate minerals via coupled dissolution-reprecipitation, that carbonates are ultimately products of mineral growth by cation dehydration from aqueous solutions and attachment to mineral surface. We acknowledge that there still a gap between the experimental system in this

study and natural carbonate-precipitating systems. Nonetheless, our study highlights the importance of distinguishing the reaction pathways as well as understanding the fundamental behavior of Mg and Ca isotopes during the classical precipitation pathway for carbonates, in order to correctly interpret metal stable isotope data from carbonate sedimentary rocks, which could be complex and diverse.

4.3.2. Implications for dolomite precipitation

Norsethite is a dolomite-analogue mineral that can form abiotically under ambient temperature (Pimentel and Pina, 2014; Lindner et al., 2018), by contrast, numerous attempts of abiotic synthesis of ordered dolomite at low temperatures were unsuccessful (e.g., Mitchell, 1923; Fairbridge, 1957; Lippmann, 1973, 1982; Land, 1998). Many hypotheses were proposed to explain this problem on dolomite (Warren, 2000), and one of the popular hypotheses is that the dehydration of Mg^{2+} aquo ion is the rate-limiting step for dolomite precipitation, due to the strong bonds between water molecules and the Mg^{2+} ion in aqueous solution (e.g., Lippmann, 1973; Land, 1998). During carbonate growth, the aquo ions need to be adsorbed onto the crystal surface and dehydrate before incorporating into crystal lattice. The hydrated Mg^{2+}-aquo ion adsorbed on to carbonate surface could block the active growth site and inhibit the further incorporation of Mg^{2+} ion into crystal (Mucci and Morse, 1983; Zhang et al., 2013; Goetschl et al., 2019), or lead to formation of certain hydrous calcium magnesium carbonate which was reported as a potential precursor for pro-dolomite (Kelleher and Redfern, 2002). More recently, various experiments were successful in synthesizing disordered dolomite with the presence of microbes (Vasconcelos et al., 1995; Petrash et al., 2017; Qiu et al., 2017), polysaccharide (Zhang et al., 2012b), dissolved sulfides in solution (Zhang et al., 2012a), and charged-clays (Liu et al., 2019). It was generally interpreted that these substances have a catalytic effect on the dehydration of Mg^{2+} aquo ion. However, the experimental results in this study show that norsethite is also formed via a precipitation pathway rather than a solid-state transition pathway, therefore, dehydration of Mg^{2+} aquo ion and incorporation of Mg^{2+} into the norsethite lattice can occur under low temperature and abiotic conditions without catalytic substances. This implies that the energy barrier for dehydration of Mg^{2+} aquo ion may not be the only key reason for the inhibition effect of Mg^{2+} aquo ion on dolomite precipitation.

The most straight forward difference between norsethite and dolomite is that Ba^{2+} has remarkably larger ionic radii than Ca^{2+} (Pimentel and Pina, 2016; Lindner et al., 2017, 2018). This causes a fine structural difference between the norsethite lattice and dolomite lattice, and results in the formation of 12-fold coordination for Ba-O polyhedra and 6-fold coordination for Ca-O octahedra, whereas Mg in both minerals forms a 6-fold coordinated Mg-O octahedra. Pimentel and Pina (2016) pointed out that difference in polyhedra of Ba^{2+} and Mg^{2+} in norsethite favors the cationic ordering during formation of norsethite structure along the c axis. This is also supported by the experiments in this study, where the newly formed norsethite already had a near-perfect cation ordering based on the near 1:1 and constant ratios of I(015)/I(110) and I(101)/(012) (Fig. 3C, D). On the other hand, Lindner and Jordan (2018) suggested that it was difficult to form a $Ba_xMg_{1-x}CO_3$ solid solution in $BaCO_3$-$MgCO_3$ system, implying that the ordered norsethite has the lowest free energy and is thermodynamically stable. Therefore, the lattice configuration of norsethite results in direct precipitation of ordered norsethite that has the lowest free energy. By contrast, both Ca and Mg has 6-fold coordination in dolomite, therefore the newly-formed dolomite tend to be disordered, and the study of Xu et al. (2013) even suggested that the distorted lattice structure in disordered dolomite facilitates incorporation of Mg^{2+} for mineral growth. The disordered dolomite, however, is not thermodynamically stable relative to ordered dolomite, thus Mg^{2+} at the surface of newly formed disordered dolomite may be easily re-hydrated and return to aqueous solution. It is likely that the difficulty in precipitation of dolomite stems from the thermodynamics and surface property of disordered dolomite, and the easiness of re-hydration of Mg on the surface of disordered dolomite.

4.3.3. Implications for the utility of the "three isotope method"

This study provides new insights for the now increasingly popular applications of "three isotope method" in experimental isotope geochemistry (e.g., Li et al., 2011, 2014, 2015; Frierdich et al., 2014a, 2014b; Zheng et al., 2016; Stamm et al., 2019). Although the three-isotope method is well-known to be a powerful method for determining isotope fractionation factors in experiments, it is also useful to distinguish reaction mechanisms. Actually, in the seminal paper by Matsuhisa et al. (1978) from R. Claytons lab at University of Chicago where the three-isotope method was invented, the authors already provided discussions in the appendix on how the combined three isotope analysis can be used to distinguish diffusion-driven exchange from recrystallization by extremely fast dissolution and reprecipitation. This point was largely neglected in numerous later three isotope method studies, but more recently Cao and Bao (2017) revived discussions on (non-)mass dependent behavior of three isotopes during exchange by different mechanisms. This study, with the surprising non-mass-dependent isotopic results, provides an exceptional first case to prove the original concept of Matsuhisa et al. (1978) that by combing isotope tracer and high precision isotopic analysis for three isotopes, one can distinguish the reaction mechanisms in a two-phases system.

5. CONCLUDING REMARKS

(1) Based on *in situ* XRD analyses, we demonstrated that formation of norsethite in a Mg-excess aqueous solution is a two-stage process that consists of precipitation of amorphous Ba-Mg carbonate precursor and subsequent transformation of amorphous carbonate (AC) to ordered norsethite without any intermediate

minerals. This is different from previous studies that reported formation of norsethite with transient occurrence of various intermediate mineral phases and dissolution of these mineral precursors. Therefore, the formation pathway of norsethite can be diverse and dependent on experimental conditions such as solution chemistry.

(2) We systematically investigated the Mg isotope exchange between Ba-Mg AC and aqueous solution during the AC transformation to norsethite using ^{25}Mg tracers, and observed surprising non-mass dependent relationship of Mg isotope data for the norsethite and aqueous solution despite very high degree of Mg isotope exchange after AC transformation. Results of numerical modeling strongly suggest that coupled dissolution-reprecipitation, rather than solid-state transition, is the key mechanism for transformation of amorphous carbonate to crystalline norsethite.

(3) This experimental study showed that norsethite can form at low temperature by direct precipitation from aqueous solution, without replacement of a mineral precursor or solid-state transformation of Ba-Mg AC. This implies that the high energy barrier of dehydration of Mg^{2+} aquo ion may not be the key reason to impede dolomite precipitation under low temperature conditions.

Declaration of Competing Interest

The authors declare that they have no known competing financial interests or personal relationships that could have appeared to influence the work reported in this paper.

ACKNOWLEDGEMENT

This paper benefited from constructive comments from S.R. Kimmig, Adrian Immenhauser and four anonymous reviewers as well as editorial handling by A. Jacobson and J. Catalano on the earlier versions of the manuscript. Yizhou Lu provided help on numerical modeling of the isotope exchange reaction; Yuguan Pan assisted in XRD analysis. Special thanks are given to Zhaofeng Zhang and Yajun An at State Key Laboratory of Isotope Geochemistry, Guangzhou Institute of Geochemistry, Chinese Science Academy, for their support in performing duplicate Mg isotope analysis for selected samples using Nu 1700 MC-ICP-MS. This study was supported by the National Natural Science Foundation of China (Grant No: 41473002; 41622301) to WL.

APPENDIX A. SUPPLEMENTARY MATERIAL

Supplementary data to this article can be found online at https://doi.org/10.1016/j.gca.2019.12.027.

REFERENCES

Addadi L., Raz S. and Weiner S. (2003) Taking advantage of disorder: Amorphous calcium carbonate and its roles in biomineralization. *Adv. Mater.* **15**, 959–970.

Aizenberg J., Lambert G., Addadi L. and Weiner S. (1996) Stabilization of amorphous calcium carbonate by specialized macromolecules in biological and synthetic precipitates. *Adv. Mater.* **8**, 222–1000.

Aizenberg J., Lambert G., Weiner S. and Addadi L. (2002) Factors involved in the formation of amorphous and crystalline calcium carbonate: A study of an ascidian skeleton. *J. Am. Chem. Soc.* **124**, 32–39.

Aizenberg J., Weiner S. and Addadi L. (2003) Coexistence of amorphous and crystalline calcium carbonate in skeletal tissues. *Connect. Tissue Res.* **44**, 20–25.

Ajikumar P. K., Wong L. G., Subramanyam G., Lakshminarayanan R. and Valiyaveettil S. (2005) Synthesis and characterization of monodispersed spheres of amorphous calcium carbonate and calcite spherules. *Cryst. Growth Des.* **5**, 1129–1134.

Al-Sawalmih A., Li C. H., Siegel S., Fratzl P. and Paris O. (2009) On the stability of amorphous minerals in lobster cuticle. *Adv. Mater.* **21**, 4011-+.

Azmy K., Lavoie D., Wang Z., Brand U., Al-Aasm I., Jackson S. and Girard I. (2013) Magnesium-isotope and REE compositions of Lower Ordovician carbonates from eastern Laurentia: Implications for the origin of dolomites and limestones. *Chem. Geol.* **356**, 64–75.

Bergquist B. A. and Blum J. D. (2007) Mass-dependent and -independent fractionation of Hg isotopes by photoreduction in aquatic systems. *Science* **318**, 417–420.

Bialik O. M., Wang X., Zhao S., Waldmann N. D., Frank R. and Li W. (2018) Mg isotope response to dolomitization in hinterland-attached carbonate platforms: Outlook of $\delta^{26}Mg$ as a tracer of basin restriction and seawater Mg/Ca ratio. *Geochim. Cosmochim. Acta* **235**, 189–207.

Blättler C. L., Miller N. R. and Higgins J. A. (2015) Mg and Ca isotope signatures of authigenic dolomite in siliceous deep-sea sediments. *Earth Planet. Sci. Lett.* **419**, 32–42.

Blue C. R. and Dove P. M. (2015) Chemical controls on the magnesium content of amorphous calcium carbonate. *Geochim. Cosmochim. Acta* **148**, 23–33.

Blue C. R., Giuffre A., Mergelsberg S., Han N., De Yoreo J. J. and Dove P. M. (2017) Chemical and physical controls on the transformation of amorphous calcium carbonate into crystalline $CaCO_3$ polymorphs. *Geochim. Cosmochim. Acta* **196**, 179–196.

Briones M. J. I., Lopez E., Mendez J., Rodriguez J. B. and Gago-Duport L. (2008) Biological control over the formation and storage of amorphous calcium carbonate by earthworms. *Mineral. Mag.* **72**, 227–231.

Burns S. J., McKenzie J. A. and Vasconcelos C. (2000) Dolomite formation and biogeochemical cycles in the Phanerozoic. *Sedimentology* **47**, 49–61.

Cao X. and Bao H. (2017) Redefining the utility of the three-isotope method. *Geochim. Cosmochim. Acta* **212**, 16–32.

Carino A., Testino A., Andalibi M. R., Pilger F., Bowen P. and Ludwig C. (2017) Thermodynamic-kinetic precipitation modeling. a case study: the amorphous calcium carbonate (ACC) precipitation pathway unravelled. *Cryst. Growth Des.* **17**, 2006–2015.

Cartwright J. H. E., Checa A. G., Gale J. D., Gebauer D. and Sainz-Diaz C. I. (2012) Calcium carbonate polyamorphism and its role in biomineralization: how many amorphous calcium carbonates are there? *Angew. Chem.-Int. Ed.* **51**, 11960–11970.

Chanda P. and Fantle M. S. (2017) Quantifying the effect of diagenetic recrystallization on the Mg isotopic composition of marine carbonates. *Geochim. Cosmochim. Acta* **204**, 219–239.

Cheng W. and Li Z. (2010) Controlled supersaturation precipitation of hydromagnesite for the $MgCl_2-Na_2CO_3$ system at

elevated temperatures: chemical modeling and experiment. *Ind. Eng. Chem. Res.* **49**, 1964–1974.

Demeny A., Nemeth P., Czuppon G., Leel-Ossy S., Szabo M., Judik K., Nemeth T. and Stieber J. (2016) Formation of amorphous calcium carbonate in caves and its implications for speleothem research. *Sci. Rep.*, 6.

Du Vivier A. D. C., Jacobson A. D., Lehn G. O., Selby D., Hurtgen M. T. and Sageman B. B. (2015) Ca isotope stratigraphy across the Cenomanian-Turonian OAE 2: Links between volcanism, seawater geochemistry, and the carbonate fractionation factor. *Earth Planet. Sci. Lett.* **416**, 121–131.

Faatz M., Gröhn F. and Wegner G. (2004) Amorphous calcium carbonate: synthesis and potential intermediate in biomineralization. *Adv. Mater.* **16**, 996–1000.

Fairbridge R. W. (1957) The dolomite question. In *Regional Aspects of Carbonate Deposition* (eds. R. J. L. Blanc and J. G. Breeding). SEPM Society for Sedimentary Geology.

Fantle M. S. and Higgins J. (2014) The effects of diagenesis and dolomitization on Ca and Mg isotopes in marine platform carbonates: Implications for the geochemical cycles of Ca and Mg. *Geochim. Cosmochim. Acta* **142**, 458–481.

Farkaš J., Buhl D., Blenkinsop J. and Veizer J. (2007) Evolution of the oceanic calcium cycle during the late Mesozoic: Evidence from δ44/40Ca of marine skeletal carbonates. *Earth Planet. Sci. Lett.* **253**, 96–111.

Farquhar J., Bao H. M. and Thiemens M. (2000) Atmospheric influence of Earth's earliest sulfur cycle. *Science* **289**, 756–758.

Frierdich A. J., Beard B. L., Reddy T. R., Scherer M. M. and Johnson C. M. (2014a) Iron isotope fractionation between aqueous Fe(II) and goethite revisited: New insights based on a multi-direction approach to equilibrium and isotopic exchange rate modification. *Geochim. Cosmochim. Acta* **139**, 383–398.

Frierdich A. J., Beard B. L., Scherer M. M. and Johnson C. M. (2014b) Determination of the Fe(II)(aq)-magnetite equilibrium iron isotope fractionation factor using the three-isotope method and a multi-direction approach to equilibrium. *Earth Planet. Sci. Lett.* **391**, 77–86.

Frierdich A. J., Nebel O., Beard B. L. and Johnson C. M. (2019) Iron isotope exchange and fractionation between hematite (α-Fe_2O_3) and aqueous Fe(II): A combined three-isotope and reversal-approach to equilibrium study. *Geochim. Cosmochim. Acta* **245**, 207–221.

Gago-Duport L., Briones M. J. I., Rodriguez J. B. and Covelo B. (2008) Amorphous calcium carbonate biomineralization in the earthworm's calciferous gland: Pathways to the formation of crystalline phases. *J. Struct. Biol.* **162**, 422–435.

Gautier Q., Bénézeth P., Mavromatis V. and Schott J. (2014) Hydromagnesite solubility product and growth kinetics in aqueous solution from 25 to 75°C. *Geochim. Cosmochim. Acta* **138**, 1–20.

Geske A., Goldstein R. H., Mavromatis V., Richter D. K., Buhl D., Kluge T., John C. M. and Immenhauser A. (2015a) The magnesium isotope (δ^{26}Mg) signature of dolomites. *Geochim. Cosmochim. Acta* **149**, 131–151.

Geske A., Lokier S., Dietzel M., Richter D. K., Buhl D. and Immenhauser A. (2015b) Magnesium isotope composition of sabkha porewater and related (Sub-)Recent stoichiometric dolomites, Abu Dhabi (UAE). *Chem. Geol.* **393–394**, 112–124.

Geske A., Zorlu J., Richter D. K., Buhl D., Niedermayr A. and Immenhauser A. (2012) Impact of diagenesis and low grade metamorphosis on isotope (delta(26)mg, delta C-13, delta O-18 and Sr-87/Sr-86) and elemental (Ca, Mg, Mn, Fe and Sr) signatures of Triassic sabkha dolomites. *Chem. Geol.* **332**, 45–64.

Giuffre A. J., Gagnon A. C., De Yoreo J. J. and Dove P. M. (2015) Isotopic tracer evidence for the amorphous calcium carbonate to calcite transformation by dissolution-reprecipitation. *Geochim. Cosmochim. Acta* **165**, 407–417.

Goetschl K. E., Purgstaller B., Dietzel M. and Mavromatis V. (2019) Effect of sulfate on magnesium incorporation in low-magnesium calcite. *Geochim. Cosmochim. Acta* **265**, 505–519.

Gong Y. U. T., Killian C. E., Olson I. C., Appathurai N. P., Amasino A. L., Martin M. C., Holt L. J., Wilt F. H. and Gilbert P. U. P. A. (2012) Phase transitions in biogenic amorphous calcium carbonate. *PNAS* **109**, 6088–6093.

Goodwin A. L., Michel F. M., Phillips B. L., Keen D. A., Dove M. T. and Reeder R. J. (2010) Nanoporous structure and medium-range order in synthetic amorphous calcium carbonate. *Chem. Mater.* **22**, 3197–3205.

Hermans J., Andre L., Navez J., Pernet P. and Dubois P. (2011) Relative influences of solution composition and presence of intracrystalline proteins on magnesium incorporation in calcium carbonate minerals: Insight into vital effects. *J. Geophys. Res.-Biogeosci.*, 116.

Higgins J. A., Blättler C. L., Lundstrom E. A., Santiago-Ramos D. P., Akhtar A. A., Crüger Ahm A. S., Bialik O., Holmden C., Bradbury H., Murray S. T. and Swart P. K. (2018) Mineralogy, early marine diagenesis, and the chemistry of shallow-water carbonate sediments. *Geochim. Cosmochim. Acta* **220**, 512–534.

Higgins J. A. and Schrag D. P. (2015) The Mg isotopic composition of Cenozoic seawater- evidence for a link between Mg-clays, seawater Mg/Ca, and climate. *Earth Planet. Sci. Lett.* **416**, 73–81.

Hood W. C., Steidl P. F. and Tschopp D. G. (1974) Precipitation of norsethite at room temperature. *Am. Mineral.* **59**, 471–474.

Hu Z., Hu W., Liu C., Sun F., Liu Y. and Li W. (2019) Conservative behavior of Mg isotopes in massive dolostones: From diagenesis to hydrothermal reworking. *Sed. Geol.* **381**, 65–75.

Hu Z., Hu W., Wang X., Lu Y., Wang L., Liao Z. and Li W. (2017) Resetting of Mg isotopes between calcite and dolomite during burial metamorphism: Outlook of Mg isotopes as geothermometer and seawater proxy. *Geochim. Cosmochim. Acta* **208**, 24–40.

Huang K.-J., Shen B., Lang X.-G., Tang W.-B., Peng Y., Ke S., Kaufman A. J., Ma H.-R. and Li F.-B. (2015) Magnesium isotopic compositions of the Mesoproterozoic dolostones: Implications for Mg isotopic systematics of marine carbonates. *Geochim. Cosmochim. Acta* **164**, 333–351.

Immenhauser A., Nägler T. F., Steuber T. and Hippler D. (2005) A critical assessment of mollusk $^{18}O/^{16}O$, Mg/Ca, and $^{44}Ca/^{40}Ca$ ratios as proxies for Cretaceous seawater temperature seasonality. *Palaeogeogr. Palaeoclimatol. Palaeoecol.* **215**, 221–237.

Jensen A. C. S., Rodriguez I., Habraken W. J. E. M., Fratzl P. and Bertinetti L. (2018) Mobility of hydrous species in amorphous calcium/magnesium carbonates. *PCCP* **20**, 19682–19688.

Jiang J., Gao M.-R., Qiu Y.-H. and Yu S.-H. (2010) Gram-scale, low-cost, rapid synthesis of highly stable Mg-ACC nanoparticles and their long-term preservation. *Nanoscale* **2**, 2358–2361.

Johnson C. M., Beard B. L. and Albarede F. (2004) Overview and general concepts. *Geochem. Non-Traditional Stable Isotopes* **55**, 1–24.

Kaczmarek S. E. and Sibley D. F. (2011) On the evolution of dolomite stoichiometry and cation order during high-temperature synthesis experiments: An alternative model for the geochemical evolution of natural dolomites. *Sed. Geol.* **240**, 30–40.

Kaczmarek S. E. and Thornton B. P. (2017) The effect of temperature on stoichiometry, cation ordering, and reaction rate in high-temperature dolomitization experiments. *Chem. Geol.* **468**, 32–41.

Katz A. and Matthews A. (1977) The dolomitization of CaCO3: an experimental study at 252–295°C. *Geochim. Cosmochim. Acta* **41**, 297–308.

Kell-Duivestein I. J., Baldermann A., Mavromatis V. and Dietzel M. (2019) Controls of temperature, alkalinity and calcium carbonate reactant on the evolution of dolomite and magnesite stoichiometry and dolomite cation ordering degree - An experimental approach. *Chem. Geol.*, 119292.

Kelleher I. J. and Redfern S. A. T. (2002) Hydrous calcium magnesium carbonate, a possible precursor to the formation of sedimentary dolomite. *Mol. Simul.* **28**, 557–572.

Koga N., Nakagoe Y. Z. and Tanaka H. (1998) Crystallization of amorphous calcium carbonate. *Thermochim. Acta* **318**, 239–244.

Königsberger E., Königsberger L.-C. and Gamsjäger H. (1999) Low-temperature thermodynamic model for the system Na_2CO_3–$MgCO_3$–$CaCO_3$–H_2O. *Geochim. Cosmochim. Acta* **63**, 3105–3119.

Konrad F., Purgstaller B., Gallien F., Mavromatis V., Gane P. and Dietzel M. (2018) Influence of aqueous Mg concentration on the transformation of amorphous calcium carbonate. *J. Cryst. Growth* **498**, 381–390.

Lam R. S. K., Charnock J. M., Lennie A. and Meldrum F. C. (2007) Synthesis-dependant structural variations in amorphous calcium carbonate. *CrystEngComm* **9**, 1226–1236.

Land L. S. (1998) Failure to precipitate dolomite at 25°C from dilute solution despite 1000-fold oversaturation after 32 years. *Aquat. Geochem.* **4**, 361–368.

Lau K. V., Maher K., Brown S. T., Jost A. B., Altıner D., DePaolo D. J., Eisenhauer A., Kelley B. M., Lehrmann D. J., Paytan A., Yu M., Silva-Tamayo J. C. and Payne J. L. (2017) The influence of seawater carbonate chemistry, mineralogy, and diagenesis on calcium isotope variations in Lower-Middle Triassic carbonate rocks. *Chem. Geol.* **471**, 13–37.

Lavoie D., Jackson S. and Girard I. (2014) Magnesium isotopes in high-temperature saddle dolomite cements in the lower Paleozoic of Canada. *Sed. Geol.* **305**, 58–68.

Lee M. R., Hodson M. E. and Langworthy G. N. (2008) Crystallization of calcite from amorphous calcium carbonate: earthworms show the way. *Mineral. Mag.* **72**, 257–261.

Levi-Kalisman Y., Raz S., Weiner S., Addadi L. and Sagi I. (2002) Structural differences between biogenic amorphous calcium carbonate phases using X-ray absorption spectroscopy. *Adv. Funct. Mater.* **12**, 43–48.

Li W., Beard B. L. and Johnson C. M. (2011) Exchange and fractionation of Mg isotopes between epsomite and saturated $MgSO_4$ solution. *Geochim. Cosmochim. Acta* **75**, 1814–1828.

Li W., Beard B. L., Li C. and Johnson C. M. (2014) Magnesium isotope fractionation between brucite [$Mg(OH)_2$] and Mg aqueous species: Implications for silicate weathering and biogeochemical processes. *Earth Planet. Sci. Lett.* **394**, 82–93.

Li W., Beard B. L., Li C., Xu H. and Johnson C. M. (2015) Experimental calibration of Mg isotope fractionation between dolomite and aqueous solution and its geological implications. *Geochim. Cosmochim. Acta* **157**, 164–181.

Li W., Bialik O. M., Wang X., Yang T., Hu Z., Huang Q., Zhao S. and Waldmann N. D. (2019) Effects of early diagenesis on Mg isotopes in dolomite: The roles of Mn(IV)-reduction and recrystallization. *Geochim. Cosmochim. Acta* **250**, 1–17.

Li W., Chakraborty S., Beard B. L., Romanek C. S. and Johnson C. M. (2012) Magnesium isotope fractionation during precipitation of inorganic calcite under laboratory conditions. *Earth Planet. Sci. Lett.* **333**, 304–316.

Lindner M. and Jordan G. (2018) On the growth of witherite and its replacement by the Mg-bearing double carbonate norsethite: Implications for the dolomite problem. *Am. Mineral.* **103**, 252–259.

Lindner M., Saldi G. D., Carrocci S., Benezeth P., Schott J. and Jordan G. (2018) On the growth of anhydrous Mg-bearing carbonates - Implications from norsethite growth kinetics. *Geochim. Cosmochim. Acta* **238**, 424–437.

Lindner M., Saldi G. D., Jordan G. and Schott J. (2017) On the effect of aqueous, barium on magnesite growth - A new route for the precipitation of the ordered anhydrous Mg-bearing double carbonate norsethite. *Chem. Geol.* **460**, 93–105.

Lippmann F. (1967) Die Synthese des Norsethits, BaMg(CO3)2, beica. 20 und 1at. ein Modell zur Dolomitisierung. *Neues Jahrb. Mineral. Monats.* **12**, 23–29.

Lippmann F. (1973) *Sedimantary Carbonate Minerals*. Springer-Verlag, Berlin Heidelberg.

Lippmann F. (1982) Stable and metastable solubility diagrams for the system $CaCO_3$ - MgCO3 -H_2O at ordinary temperature. *Bulletin De Mineralogie* **105**, 273–279.

Liu D., Xu Y., Papineau D., Yu N., Fan Q., Qiu X. and Wang H. (2019) Experimental evidence for abiotic formation of low-temperature proto-dolomite facilitated by clay minerals. *Geochim. Cosmochim. Acta*.

Long X., Ma Y. and Qi L. (2011) In vitro synthesis of high Mg calcite under ambient conditions and its implication for biomineralization process. *Cryst. Growth Des.* **11**, 2866–2873.

Loste E., Wilson R. M., Seshadri R. and Meldrum F. C. (2003) The role of magnesium in stabilising amorphous calcium carbonate and controlling calcite morphologies. *J. Cryst. Growth* **254**, 206–218.

Martignier A., Pacton M., Filella M., Jaquet J. M., Barja F., Pollok K., Langenhorst F., Lavigne S., Guagliardo P., Kilburn M. R., Thomas C., Martini R. and Ariztegui D. (2017) Intracellular amorphous carbonates uncover a new biomineralization process in eukaryotes. *Geobiology* **15**, 240–253.

Mass T., Giuffre A. J., Sun C.-Y., Stifler C. A., Frazier M. J., Neder M., Tamura N., Stan C. V., Marcus M. A. and Gilbert P. U. P. A. (2017) Amorphous calcium carbonate particles form coral skeletons. *PNAS* **114**, E7670–E7678.

Matsuhisa Y., Goldsmith J. R. and Clayton R. N. (1978) Mechanisms of hydrothermal crystallization of quartz at 250 and 15 kbar. *Geochim. Cosmochim. Acta* **42**, 173–1000.

Matthews A., Goldsmith J. R. and Clayton R. N. (1983) On the mechanisms and kinetics of oxygen isotope exchange in quartz and feldspars at elevated-temperatures and pressure. *Geol. Soc. Am. Bull.* **94**, 396–412.

Mavromatis V., Harrison A. L., Eisenhauer A. and Dietzel M. (2017a) Strontium isotope fractionation during strontianite ($SrCO_3$) dissolution, precipitation and at equilibrium. *Geochim. Cosmochim. Acta* **218**, 201–214.

Mavromatis V., Meister P. and Oelkers E. H. (2014) Using stable Mg isotopes to distinguish dolomite formation mechanisms: A case study from the Peru Margin. *Chem. Geol.* **385**, 84–91.

Mavromatis V., Purgstaller B., Dietzel M., Buhl D., Immenhauser A. and Schott J. (2017b) Impact of amorphous precursor phases on magnesium isotope signatures of Mg-calcite. *Earth Planet. Sci. Lett.* **464**, 227–236.

Mavromatis V., van Zuilen K., Purgstaller B., Baldermann A., Nagler T. F. and Dietzel M. (2016) Barium isotope fractionation during witherite ($BaCO_3$) dissolution, precipitation and at equilibrium. *Geochim. Cosmochim. Acta* **190**, 72–84.

Mitchell A. E. (1923) Studies on the dolomite system - Part II. *J. Chem. Soc.* **123**, 1887–1904.

Montes-Hernandez G., Findling N. and Renard F. (2016) Dissolution-precipitation reactions controlling fast formation of dolomite under hydrothermal conditions. *Appl. Geochem.* **73**, 169–177.

Morrow D. W. and Ricketts B. D. (1986) Chemical controls on the precipitation of mineral analogues of dolomite: The sulfate enigma. *Geology* **14**, 408–410.

Mucci A. and Morse J. W. (1983) The incorporation of Mg2+ and Sr2+ into calcite overgrowths: influences of growth rate and solution composition. *Geochim. Cosmochim. Acta* **47**, 217–233.

Müller M. N., Kısakürek B., Buhl D., Gutperlet R., Kolevica A., Riebesell U., Stoll H. and Eisenhauer A. (2011) Response of the coccolithophores Emiliania huxleyi and Coccolithus braarudii to changing seawater Mg2+ and Ca2+ concentrations: Mg/Ca, Sr/Ca ratios and δ44/40Ca, δ26/24Mg of coccolith calcite. *Geochim. Cosmochim. Acta* **75**, 2088–2102.

Nudelman F., Sonmezler E., Bomans P. H. H., de With G. and Sommerdijk N. A. J. M. (2010) Stabilization of amorphous calcium carbonate by controlling its particle size. *Nanoscale* **2**, 2436–2439.

Oelkers E. H., von Strandmann P. A. E. P. and Mavromatis V. (2019) The rapid resetting of the Ca isotopic signatures of calcite at ambient temperature during its congruent dissolution, precipitation, and at equilibrium. *Chem. Geol.* **512**, 1–10.

Ogino T., Suzuki T. and Sawada K. (1987) The formation and transformation mechanism of calcium carbonate in water. *Geochim. Cosmochim. Acta* **51**, 2757–2767.

Ono S., Eigenbrode J. L., Pavlov A. A., Kharecha P., Rumble D., Kasting J. F. and Freeman K. H. (2003) New insights into Archean sulfur cycle from mass-independent sulfur isotope records from the Hamersley Basin, Australia. *Earth Planet. Sci. Lett.* **213**, 15–30.

Petrash D. A., Bialik O. M., Bontognali T. R. R., Vasconcelos C., Roberts J. A., McKenzie J. A. and Konhauser K. O. (2017) Microbially catalyzed dolomite formation: From near-surface to burial. *Earth-Sci. Rev.* **171**, 558–582.

Pimentel C. and Pina C. M. (2014) The formation of the dolomite-analogue norsethite: Reaction pathway and cation ordering. *Geochim. Cosmochim. Acta* **142**, 217–223.

Pimentel C. and Pina C. M. (2016) Reaction pathways towards the formation of dolomite-analogues at ambient conditions. *Geochim. Cosmochim. Acta* **178**, 259–267.

Point D., Sonke J. E., Day R. D., Roseneau D. G., Hobson K. A., Vander Pol S. S., Moors A. J., Pugh R. S., Donard O. F. X. and Becker P. R. (2011) Methylmercury photodegradation influenced by sea-ice cover in Arctic marine ecosystems. *Nat. Geosci.* **4**, 188–194.

Politi Y., Batchelor D. R., Zaslansky P., Chmelka B. F., Weaver J. C., Sagi I., Weiner S. and Addadi L. (2010) Role of magnesium ion in the stabilization of biogenic amorphous calcium carbonate: a structure-function investigation. *Chem. Mater.* **22**, 161–166.

Politi Y., Levi-Kalisman Y., Raz S., Wilt F., Addadi L., Weiner S. and Sagi I. (2006) Structural characterization of the transient amorphous calcium carbonate precursor phase in sea urchin embryos. *Adv. Funct. Mater.* **16**, 1289–1298.

Politi Y., Metzler R. A., Abrecht M., Gilbert B., Wilt F. H., Sagi I., Addadi L., Weiner S. and Gilbert P. U. P. A. (2008) Transformation mechanism of amorphous calcium carbonate into calcite in the sea urchin larval spicule (vol 105, pg 17362, 2008). *Proc. Natl. Acad. Sci. U. S. A.* **105**, 20045-20045.

Purgstaller B., Goetschl K. E., Mavromatis V. and Dietzel M. (2019) Solubility investigations in the amorphous calcium magnesium carbonate system. *CrystEngComm* **21**, 155–164.

Purgstaller B., Konrad F., Dietzel M., Immenhauser A. and Mavromatis V. (2017) Control of Mg^{2+}/Ca^{2+} activity ratio on the formation of crystalline carbonate minerals via an amorphous precursor. *Cryst. Growth Des.* **17**, 1069–1078.

Purgstaller B., Mavromatis V., Immenhauser A. and Dietzel M. (2016) Transformation of Mg-bearing amorphous calcium carbonate to Mg-calcite - In situ monitoring. *Geochim. Cosmochim. Acta* **174**, 180–195.

Qiu X., Wang H., Yao Y. and Duan Y. (2017) High salinity facilitates dolomite precipitation mediated by Haloferax volcanii DS52. *Earth Planet. Sci. Lett.* **472**, 197–205.

Radha A. V., Fernandez-Martinez A., Hu Y., Jun Y.-S., Waychunas G. A. and Navrotsky A. (2012) Energetic and structural studies of amorphous $Ca_{1-x}Mg_xCO_3 \bullet nH_2O$ ($0 \leq x \leq 1$). *Geochim. Cosmochim. Acta* **90**, 83–95.

Raz S., Hamilton P. C., Wilt F. H., Weiner S. and Addadi L. (2003) The transient phase of amorphous calcium carbonate in sea urchin larval spicules: The involvement of proteins and magnesium ions in its formation and stabilization. *Adv. Funct. Mater.* **13**, 480–486.

Raz S., Weiner S. and Addadi L. (2000) Formation of high-magnesian calcites via an amorphous precursor phase: Possible biological implications. *Adv. Mater.* **12**, 38-+.

Riechelmann S., Mavromatis V., Buhl D., Dietzel M., Eisenhauer A. and Immenhauser A. (2016) Impact of diagenetic alteration on brachiopod shell magnesium isotope (δ26Mg) signatures: Experimental versus field data. *Chem. Geol.* **440**, 191–206.

Riechelmann S., Mavromatis V., Buhl D., Dietzel M., Hoffmann R., Jöns N., Kell-Duivestein I. and Immenhauser A. (2018) Echinoid skeletal carbonate as archive of past seawater magnesium isotope signatures – Potential and limitations. *Geochim. Cosmochim. Acta* **235**, 333–359.

Rodriguez-Blanco J. D., Shaw S. and Benning L. G. (2008) How to make 'stable' ACC: protocol and preliminary structural characterization. *Mineral. Mag.* **72**, 283–286.

Rodriguez-Blanco J. D., Shaw S. and Benning L. G. (2011) The kinetics and mechanisms of amorphous calcium carbonate (ACC) crystallization to calcite, via vaterite. *Nanoscale* **3**, 265–271.

Rodriguez-Blanco J. D., Shaw S., Bots P., Roncal-Herrero T. and Benning L. G. (2012) The role of pH and Mg on the stability and crystallization of amorphous calcium carbonate. *J. Alloy. Compd.* **536**, S477–S479.

Rodriguez-Blanco J. D., Shaw S., Bots P., Roncal-Herrero T. and Benning L. G. (2014) The role of Mg in the crystallization of monohydrocalcite. *Geochim. Cosmochim. Acta* **127**, 204–220.

Rodriguez-Navarro C., Kudlacz K., Cizer O. and Ruiz-Agudo E. (2015) Formation of amorphous calcium carbonate and its transformation into mesostructured calcite. *CrystEngComm* **17**, 58–72.

Schultzguttler R. (1986) The influence of disordered, non-equilibrium dolomites on the Mg-solubility in calcite in the system $CaCO_3$-$MgCO_3$. *Contrib. Mineral. Petrol.* **93**, 395–398.

Sherman L. S., Blum J. D., Johnson K. P., Keeler G. J., Barres J. A. and Douglas T. A. (2010) Mass-independent fractionation of mercury isotopes in Arctic snow driven by sunlight. *Nat. Geosci.* **3**, 173–177.

Sibley D. F., Dedoes R. E. and Bartlett T. R. (1987) Kinetics of dolomitization. *Geology* **15**, 1112–1114.

Singer J. W., Yazaydin A. O., Kirkpatrick R. J. and Bowers G. M. (2012) Structure and transformation of amorphous calcium carbonate: a solid-state ^{43}Ca NMR and computational molecular dynamics investigation. *Chem. Mater.* **24**, 1828–1836.

Skierszkan E. K., Mayer K. U., Weis D., Roberston J. and Beckie R. D. (2019) Molybdenum stable isotope fractionation during the precipitation of powellite ($CaMoO_4$) and wulfenite ($PbMoO_4$). *Geochim. Cosmochim. Acta* **244**, 383–402.

Stamm F. M., Zambardi T., Chmeleff J., Schott J., von Blanckenburg F. and Oelkers E. H. (2019) The experimental determination of equilibrium Si isotope fractionation factors among $H_4SiO_4^0$, $H_3SiO_4^-$ and amorphous silica ($SiO_2 \cdot 0.32\ H_2O$) at 25 and 75 °C using the three-isotope method. *Geochim. Cosmochim. Acta* **255**, 49–68.

Steuber T. and Buhl D. (2006) Calcium-isotope fractionation in selected modern and ancient marine carbonates. *Geochim. Cosmochim. Acta* **70**, 5507–5521.

Stipp S. L. S., Konnerup-Madsen J., Franzreb K., Kulik A. and Mathieu H. J. (1998) Spontaneous movement of ions through calcite at standard temperature and pressure. *Nature* **396**, 356–359.

Thiemens M. H. (1999) Atmosphere science – Mass-independent isotope effects in planetary atmospheres and the early solar system. *Science* **283**, 341–345.

Vasconcelos C., McKenzie J. A., Bernasconi S., Grujic D. and Tien A. J. (1995) Microbial mediation as a possible mechanism for natural dolomite formation at low temperatures. *Nature* **377**, 220–222.

Walter B. F., Immenhauser A., Geske A. and Markl G. (2015) Exploration of hydrothermal carbonate magnesium isotope signatures as tracers for continental fluid aquifers, Schwarzwald mining district, SW Germany. *Chem. Geol.* **400**, 87–105.

Wang D., Hamm L. M., Bodnar R. J. and Dove P. M. (2011) Raman spectroscopic characterization of the magnesium content in amorphous calcium carbonates. *J. Raman Spectrosc.* **43**, 543–548.

Wang D. B., Wallace A. F., De Yoreo J. J. and Dove P. M. (2009) Carboxylated molecules regulate magnesium content of amorphous calcium carbonates during calcification. *PNAS* **106**, 21511–21516.

Wang J., Jacobson A. D., Zhang H., Ramezani J., Sageman B. B., Hurtgen M. T., Bowring S. A. and Shen S.-Z. (2019) Coupled $\delta^{44/40}$Ca, $\delta^{88/86}$Sr, and ^{87}Sr/^{86}Sr geochemistry across the end-Permian mass extinction event. *Geochim. Cosmochim. Acta*.

Wang Y. W., Kim Y. Y., Stephens C. J., Meldrum F. C. and Christenson H. K. (2012) In situ study of the precipitation and crystallization of amorphous calcium carbonate (ACC). *Cryst. Growth Des.* **12**, 1212–1217.

Warren J. (2000) Dolomite: occurrence, evolution and economically important associations. *Earth-Sci. Rev.* **52**, 1–81.

Weiner S. and Addadi L. (2011) Crystallization pathways in biomineralization. *Annu. Rev. Mater. Res.* **41**(41), 21–40.

Weiner S., Levi-Kalisman Y., Raz S. and Addadi L. (2003) Biologically formed amorphous calcium carbonate. *Connect. Tissue Res.* **44**, 214–218.

Weiss I. M., Tuross N., Addadi L. and Weiner S. (2002) Mollusc larval shell formation: Amorphous calcium carbonate is a precursor phase for aragonite. *J. Exp. Zool.* **293**, 478–491.

Xiong Y. (2011) Experimental determination of solubility constant of hydromagnesite (5424) in NaCl solutions up to 4.4m at room temperature. *Chem. Geol.* **284**, 262–269.

Xu J., Yan C., Zhang F., Konishi H., Xu H. and Teng H. H. (2013) Testing the cation-hydration effect on the crystallization of Ca-Mg-CO_3 systems. *PNAS* **110**, 17750–17755.

Yang S.-Y., Chang H.-H., Lin C.-J., Huang S.-J. and Chan J. C. C. (2016) Is Mg-stabilized amorphous calcium carbonate a homogeneous mixture of amorphous magnesium carbonate and amorphous calcium carbonate? *Chem. Commun.* **52**, 11527–11530.

Young E. D., Galy A. and Nagahara H. (2002) Kinetic and equilibrium mass-dependent isotope fractionation laws in nature and their geochemical and cosmochemical significance. *Geochim. Cosmochim. Acta* **66**, 1095–1104.

Zhang F., Xu H., Konishi H., Kemp J. M., Roden E. E. and Shen Z. (2012a) Dissolved sulfide-catalyzed precipitation of disordered dolomite: Implications for the formation mechanism of sedimentary dolomite. *Geochim. Cosmochim. Acta* **97**, 148–165.

Zhang F., Xu H., Konishi H., Shelobolina E. S. and Roden E. E. (2012b) Polysaccharide-catalyzed nucleation and growth of disordered dolomite: A potential precursor of sedimentary dolomite. *Am. Mineral.* **97**, 556–567.

Zhang F., Yan C., Teng H. H., Roden E. E. and Xu H. (2013) In situ AFM observations of Ca–Mg carbonate crystallization catalyzed by dissolved sulfide: Implications for sedimentary dolomite formation. *Geochim. Cosmochim. Acta* **105**, 44–55.

Zheng X.-Y., Beard B. L. and Johnson C. M. (2019) Constraining silicon isotope exchange kinetics and fractionation between aqueous and amorphous Si at room temperature. *Geochim. Cosmochim. Acta* **253**, 267–289.

Zheng X.-Y., Beard B. L., Reddy T. R., Roden E. E. and Johnson C. M. (2016) Abiologic silicon isotope fractionation between aqueous Si and Fe(III)-Si gel in simulated Archean seawater: Implications for Si isotope records in Precambrian sedimentary rocks. *Geochim. Cosmochim. Acta* **187**, 102–122.s.

Zou Z. Y., Bertinetti L., Politi Y., Jensen A. C. S., Weiner S., Addadi L., Fratzl P. and Habraken W. (2015) Opposite particle size effect on amorphous calcium carbonate crystallization in water and during heating in air. *Chem. Mater.* **27**, 4237–4246.

Associate editor: Andrew D. Jacobson